Bulletin of Mathematical Biology (2010) 72: 400–431
DOI 10.1007/s11538-009-9452-4

ORIGINAL ARTICLE

On the Modelling of Biological Patterns with Mechanochemical Models: Insights from Analysis and Computation

P. Moreo[a,c,*], E.A. Gaffney[d,e], J.M. García-Aznar[a,b], M. Doblaré[a,b]

[a] *Group of Structural Mechanics and Materials Modelling, Aragón Institute of Engineering Research, University of Zaragoza, Zaragoza, Spain*
[b] *CIBER-BBN Centro de Investigación Biomédica en Red En Bioingeniería, Biomateriales y Nanomedicina, Aragón Institute of Health Sciences, Zaragoza, Spain*
[c] *EBERS Medical Technology S.L., Zaragoza, Spain*
[d] *Centre for Mathematical Biology, Mathematical Institute, University of Oxford, Oxford, UK*
[e] *Oxford Centre for Collaborative Applied Mathematics, Mathematical Institute, University of Oxford, Oxford, UK*

Received: 24 February 2009 / Accepted: 14 August 2009 / Published online: 14 November 2009

Abstract The diversity of biological form is generated by a relatively small number of underlying mechanisms. Consequently, mathematical and computational modelling can, and does, provide insight into how cellular level interactions ultimately give rise to higher level structure. Given cells respond to mechanical stimuli, it is therefore important to consider the effects of these responses within biological self-organisation models. Here, we consider the self-organisation properties of a mechanochemical model previously developed by three of the authors in Acta Biomater. 4, 613–621 (2008), which is capable of reproducing the behaviour of a population of cells cultured on an elastic substrate in response to a variety of stimuli. In particular, we examine the conditions under which stable spatial patterns can emerge with this model, focusing on the influence of mechanical stimuli and the interplay of non-local phenomena. To this end, we have performed a linear stability analysis and numerical simulations based on a mixed finite element formulation, which have allowed us to study the dynamical behaviour of the system in terms of the qualitative shape of the dispersion relation. We show that the consideration of mechanotaxis, namely changes in migration speeds and directions in response to mechanical stimuli alters the conditions for pattern formation in a singular manner. Furthermore without non-local effects, responses to mechanical stimuli are observed to result in dispersion relations with positive growth rates at arbitrarily large wavenumbers, in turn yielding heterogeneity at the cellular level in model predictions. This highlights the sensitivity and necessity of non-local effects in mechanically influenced biological

*Corresponding author.
E-mail addresses: pmoreo@unizar.es (P. Moreo), gaffney@maths.ox.ac.uk (E.A. Gaffney), jmgaraz@unizar.es (J.M. García-Aznar), mdoblare@unizar.es (M. Doblaré).

pattern formation models and the ultimate failure of the continuum approximation in their absence.

Keywords Pattern formation · Finite element simulation

1. Introduction

The appearance of spatiotemporal patterns in dynamical systems driven away from equilibrium is due to the emergence of symmetry-breaking bifurcations (Cross and Hohenberg, 1993). These can be classified on the basis of a linear stability analysis of a homogeneous steady state, revealing three types of instabilities: (1) oscillations uniform in space and periodic in time that emerge due to a Hopf bifurcation; (2) patterns stationary in time and oscillatory in space, after a Turing bifurcation; and (3) patterns oscillatory in both time and space, resulting from a wave bifurcation (Yang et al., 2002). There are numerous situations of great interest where spatiotemporal patterns arise and play an important role; these include fluid dynamics (Cross and Hohenberg, 1993), chemical reactions (Field and Burger, 1985), solidification (Flesselles et al., 1991), non-linear optics (Moloney and Newell, 1990), and biological systems (Turing, 1952; Murray, 1989).

In particular, two broad classes of spatial patterns are pre-eminent in biological phenomena: time-dependent patterns, involving propagating waves, and stationary patterns, typical of morphogenesis. Examples of the former include pulse propagation in nerves (Hodgkin and Huxley, 1952; FitzHugh, 1961; Nagumo et al., 1962) and cardiac electrophysiology (Glass and Hunter, 1990; Hunter et al., 2003). As reviewed by Murray (1989), stationary pattern formation has been investigated extensively as the driving mechanism for numerous morphogenetic self-organisation systems including: the regeneration and transplantation in hydra (Gierer and Meinhardt, 1972), mammalian coat markings (Murray, 1981a, 1981b), pigment patterns on mollusc shells (Meinhardt et al., 2003), periodic patterns of feather germs, and cartilage condensations in limb morphogenesis (Murray and Oster, 1984; Miura et al., 2006).

Two fundamental theoretical paradigms have been proposed as frameworks for understanding the underlying mechanisms involved in morphogenesis. The first is Wolpert's phenomenological French flag concept of positional information, which hypothesises that a spatial pattern of chemicals called morphogens initially develops and subsequently drives a heterogeneous cell response (Wolpert, 1969). In this approach, pattern formation and morphogenesis take place sequentially. An alternative view on biological pattern generation, pioneered in Oster et al. (1983), comes from the so-called mechanochemical approach, as reviewed by Murray et al. (1988). The important additional feature of these models is the consideration of the effect of mechanical forces exerted by cells on the deformation of the underlying extracellular matrix. Thus, pattern formation and morphogenesis are coupled. While originally proposed for the modelling of mesenchymal morphogenesis, this framework has also been applied to the formation of vascular networks (Manoussaki, 2003; Namy et al., 2004), the epithelium (Mittenthal and Mazo, 1983), and tumour angiogenesis (Holmes and Sleeman, 2000). A core feature and theoretical advantage of this approach is the interaction between mechanics and geometry, i.e. form,

allowing potential self correcting mechanisms, crucial for embryonic development (Murray et al., 1988). However, the ensuing models are considerably more complex than those involving pure reaction and diffusion. In particular, in pattern formation studies, they generally exhibit complicated linear dispersion relations with diverging growth rates at large wavenumbers that can only be avoided by the addition of long range effects (Murray, 1989).

We must emphasise that mechanochemical models that couple, on the one hand, the mechanical behaviour of an underlying extracellular matrix (ECM) or substrate, by means of the balance of linear momentum and constitutive equations; and, on the other hand, the evolution of a population of cells living on the ECM, by means of reaction-diffusion equations, have applications that stretch much further than morphogenesis in development biology. Any theoretical effort aimed at modelling the influence of mechanics or topography on cell migration, proliferation, and differentiation from a continuum perspective is especially suited to such a framework. Such phenomena are common and diverse (Schwarz and Bischofs, 2005): cells tend to orient along directions of ECM fibres (contact guidance); they also have a propensity to navigate in the ECM in response to its mechanical resistance (mechanotaxis) and to migrate in favour of stiffer (durotaxis) or strained (tensotaxis) substrates; they can also proliferate at a rate dependent on the stiffness of the substrate (Ghosh et al., 2007) and differentiate in response to the mechanical stimuli they are able to sense (Pavlin et al., 2000; Cullinane et al., 2003); finally, they can adhere to surfaces in a topography dependent manner (Park et al., 2001). The number of medical and biological situations where these mechanical effects play a decisive role is enormous: tissue engineering, bone fracture healing, endosseous implant osseointegration, and wound healing, among many others. Such applications are driving a research programme aimed at developing our understanding of, and our ability to simulate, mechanochemical models. This is exemplified by Moreo et al. (2008), where three of the current authors developed a mechanochemical model with the aim of investigating the numerous influences of mechanics on cell behaviour and proliferation. In particular, this study considered the variation of forces exerted by cells due to the mechanical state of the ECM, and was able to reproduce the effects of durotaxis and tensotaxis as well as including the influence of ECM stiffness on the rate of cell proliferation.

Note that the numerical treatment of fully coupled mechanochemical models has commonly been addressed via finite difference techniques, with all the limitations that this approach involves, especially in resolving domains with complex geometries, typical of biological problems. A few works have proposed more versatile computational implementations (see, for example, Garikipati et al., 2004).

Hence, the objective of the current study is to investigate and delimit conditions for biological self-organisation in the above mentioned mechanochemical model of Moreo et al. (2008), in particular focussing on the influence of long range effects, such as durotaxis/tensotaxis. Thus, a linear stability analysis of the model around the homogeneous steady state of interest has been implemented in conjunction with a numerical simulation via a mixed finite element formulation.

The linear stability analysis yields numerous generic insights and conclusions concerning the interplay among long range phenomena, haptotaxis, durotaxis/tensotaxis and cell forces in self-organisation. The computational simulations additionally validate the linear analysis sufficiently close to the homogeneous steady state of relevance. They also

illustrate the robustness of the pattern shape to randomness in the initial conditions and show that dispersion relations with positive growth rates at arbitrarily large wavenumber give rise to pattern at arbitrarily small wavelength, where the limit of validity of any continuum model is reached.

2. Description of the model

As previously mentioned, the model proposed in this section is an extension of the mechanochemical model presented in Moreo et al. (2008), which was designed to examine the interaction of a cell population with a surrounding tissue. The two main features of the model are:

- Unlike most existing mechanobiological models, an expression for the cellular flux is not directly postulated, but motivated from thermodynamic arguments (see Doblaré and García-Aznar, 2005 for a detailed description of this procedure). Using this approach, a new term appears in the cellular flux that depends on cell forces applied on the matrix which reproduces the well-known phenomena of durotaxis and tensotaxis.
- The traction p_{cell} exerted on the ECM per cell is no longer assumed to be constant. According to recent experimental evidence, it is clear that adherent cells anchor to a substrate and then exert contractile forces to explore the properties of their environment, which is integral to the process of mechanosensing (Discher et al., 2005). The magnitude of the forces exerted by a cell signals the stiffness and strain of the substrate to which the cell is anchored. Therefore, the forces denoted by p_{cell} are not constant. In the modelling, as detailed below, an expression for p_{cell} is considered which represents the active behaviour of the actomyosin contractile machinery and the passive behaviour of the mechanically relevant constituents of the cell.

In Section 2.1, we introduce the strong form of the model. Next, in Sections 2.2–2.4, a basic discussion on the biological and mechanical basis of each model equation is given. The reader is referred to Moreo et al. (2008) for further details concerning the physical interpretation of the equations. Finally, some model assumptions are further discussed in Section 2.5.

2.1. Strong form of the model

The main variables of the model are the cellular concentration, n, the displacement of the ECM, $\mathbf{u}$, and the density of the ECM, ρ, which are functions of time t and the spatial position $\mathbf{x}$. A continuum approach is followed, and consequently the model is based on fundamental conservation equations for n and ρ and the balance of linear momentum for the ECM. Furthermore the hypothesis of small strains and displacements is assumed throughout the text.

Under these assumptions, let the domain be an open, simply connected region in space Ω. The boundary of Ω is supposed to be sufficiently smooth, and is denoted by $\Gamma = \partial\Omega$, with outward unit normal $\boldsymbol{\eta}$. Further, let $\Gamma = \overline{\Gamma_g \cup \Gamma_m} = \overline{\Gamma_q \cup \Gamma_l}$, where $\Gamma_g \cap \Gamma_m = \Gamma_q \cap \Gamma_l = \emptyset$.

In the strong form, we have the following problem:

Find $n, \rho : \overline{\Omega} \times [0, T] \longrightarrow \mathbb{R}$, $\mathbf{u} : \overline{\Omega} \times [0, T] \longrightarrow \mathbb{R}^3$ such that

$$\frac{\partial n}{\partial t} + \nabla \cdot \left[-D_1 \nabla n + D_2 \nabla\left(\nabla^2 n\right) + h_1 n \nabla \rho - h_2 n \nabla\left(\nabla^2 \rho\right) + n \frac{\partial \mathbf{u}}{\partial t} + M \nabla \cdot \boldsymbol{\sigma}_{\text{cell}} \right] = r(\theta) n \left(1 - \frac{n}{N}\right), \tag{1}$$

$$\frac{\partial \rho}{\partial t} + \nabla \cdot \left[\rho \frac{\partial \mathbf{u}}{\partial t} \right] = 0, \tag{2}$$

$$\nabla \cdot \left[\boldsymbol{\sigma}_{\text{ecm}}(\mathbf{u}) + \boldsymbol{\sigma}_{\text{cell}}(\mathbf{u}) \right] + \rho \mathbf{f}_{\text{ext}} = \mathbf{0}, \tag{3}$$

on $\Omega \times (0, T)$, where $\theta \stackrel{\text{def}}{=} \nabla \cdot \mathbf{u}$ and D_1, D_2, h_1, h_2, M, N are non-negative parameters.

We further impose the following boundary conditions (Wells et al., 2006):

$$n = g \quad \text{on } \Gamma_g \times (0, T), \tag{4}$$

$$\nabla n \cdot \boldsymbol{\eta} = q \quad \text{on } \Gamma_q \times (0, T), \tag{5}$$

$$\nabla^2 n = l \quad \text{on } \Gamma_l \times (0, T), \tag{6}$$

$$\mathbf{J}_n \cdot \boldsymbol{\eta} = m \quad \text{on } \Gamma_m \times (0, T), \tag{7}$$

$$\mathbf{u} = \mathbf{0} \quad \text{on } \Gamma \times (0, T). \tag{8}$$

Finally, we have the initial conditions:

$$n(\mathbf{x}, 0) = n_0(\mathbf{x}) \quad \text{in } \Omega, \tag{9}$$

$$\rho(\mathbf{x}, 0) = \rho_0(\mathbf{x}) \quad \text{in } \Omega, \tag{10}$$

where $\mathbf{J}_n$ is the total flux of Eq. (1). Note that the boundary condition (8) implies that the normal flux of ρ on Γ is zero, so no extra boundary condition is needed for ρ.

2.2. *Cell concentration* $n(\mathbf{x}, t)$

Coefficients D_1 and D_2 of Eq. (1) characterise short and long range diffusion, respectively, and h_1 and h_2 stand for short and long range haptotaxis parameters. M is a coefficient that quantifies the influence of mechanical stimuli on the direction and magnitude of cell migration velocity. Finally, the source term describes the kinetics of the cellular population by means of a simple logistic growth law with maximum carrying capacity N and rate of cell proliferation r dependent on the ECM volumetric strain $\theta \stackrel{\text{def}}{=} \nabla \cdot \mathbf{u}$. Note that the flux term that depends on the temporal derivative of the ECM displacement accounts for passive convection, i.e. since cells are attached to the ECM, they flow passively as a consequence of its deformation.

Observe that the flux term that depends on the divergence of the cellular stress tensor $\boldsymbol{\sigma}_{\text{cell}}$ is responsible for a preferential migration of cells towards more strained or stiffer areas. It is reasonable to assume that under low cell densities $\boldsymbol{\sigma}_{\text{cell}}$ is proportional to the force applied by a single cell p_{cell} and to the local cell density n. However, at high cell

densities $\boldsymbol{\sigma}_{\text{cell}}$ tends to saturate or even decrease. Additionally, the fact that cellular filopodia can extend beyond their immediate neighbourhood prompts us to include a non-local effect, in the sense that $\boldsymbol{\sigma}_{\text{cell}}$ depends not only on the local cell density n, but also on the average density of the local neighbourhood, measured by $\nabla^2 n$ (Murray, 1989). Hence, the following expression is proposed:

$$\boldsymbol{\sigma}_{\text{cell}} = p_{\text{cell}} \frac{n + \beta \nabla^2 n}{1 + \lambda n^2} \mathbf{I}, \tag{11}$$

where λ characterises the cellular stress saturation, β is a measure of the non-local effect and $\mathbf{I}$ the second order identity tensor. Note that we are assuming that forces exerted by cells are isotropic, which should be considered as a first approximation in model development.

The active pressure p_{cell} transmitted to the ECM by a single cell is a continuous function of the ECM volumetric strain θ (Moreo et al., 2008):

$$p_{\text{cell}} = \begin{cases} K_{\text{pas}}\theta, & \theta < \theta_1, \\ \frac{K_{\text{act}} p_{\max}}{K_{\text{act}}\theta_1 - p_{\max}}(\theta_1 - \theta) + K_{\text{pas}}\theta, & \theta_1 \leq \theta \leq \theta^*, \\ \frac{K_{\text{act}} p_{\max}}{K_{\text{act}}\theta_2 - p_{\max}}(\theta_2 - \theta) + K_{\text{pas}}\theta, & \theta^* < \theta \leq \theta_2, \\ K_{\text{pas}}\theta & \theta > \theta_2, \end{cases} \tag{12}$$

where K_{act} and K_{pas} stand for the stiffness of the active and passive constituents of the cell, $p_{\max}$ denotes the maximum contractile force that can be generated by the actomyosin machinery, $\theta_1 < 0$ and $\theta_2 > 0$ are the corresponding shortening and lengthening strains of the contractile machinery at which active stress becomes zero and $\theta^* = p_{\max}/K_{\text{act}} > 0$. Equation (12) basically states that when the volumetric strain θ lies in the range $\theta_1 < \theta < \theta_2$ cells are able to develop and transmit active force to the ECM. Outside this range, cells simply attach to the ECM and become deformed passively together with it, but they are not able to generate active forces and thus simply experience passive stresses. The latter arise from the deformation of the membrane and other passive elements of the cytoskeleton with relevant mechanical function.

Finally, it has been shown that certain types of cells proliferate markedly faster on substrates where they exert higher tractional forces (see, for example Ghosh et al., 2007 for human fibroblasts). Accordingly, we propose the following expression for r:

$$r(\theta) = r_{\max} \frac{p_{\text{cell}}(\theta)}{p_{\text{cell}}(\theta) + \tau}, \tag{13}$$

where $r_{\max}$ stands for the maximum rate of cell proliferation and τ is a parameter that characterises the dependence of r upon p_{cell}.

2.3. *ECM density* $\rho(\mathbf{x}, t)$

In the case of the ECM density, we consider that the only flux term comes from passive convection and that the secretion of ECM by cells is not relevant as a first approximation and thus no source term appears in Eq. (2).

2.4. *ECM displacement* $\mathbf{u}(\mathbf{x}, t)$

The balance of linear momentum of Eq. (3) states that the passive ECM stresses $\boldsymbol{\sigma}_{\text{ecm}}$, which appear as a result of deformation of the ECM, are in equilibrium with the external applied forces per unit mass $\mathbf{f}_{\text{ext}}$ and the applied stresses exerted by the cellular population adhered to the ECM, $\boldsymbol{\sigma}_{\text{cell}}$. Without loss of generality, we will assume a general linear viscoelastic mechanical behaviour for the ECM, and hence

$$\boldsymbol{\sigma}_{\text{ecm}} = \frac{E}{1+\nu}\left(\boldsymbol{\varepsilon} + \frac{\nu}{1-2\nu}\theta\mathbf{I}\right) + \mu_1\frac{\partial \boldsymbol{\varepsilon}}{\partial t} + \mu_2\frac{\partial \theta}{\partial t}\mathbf{I}, \tag{14}$$

where $\boldsymbol{\varepsilon}$ is the ECM strain tensor—under the small strains assumption, $\boldsymbol{\varepsilon} = \frac{1}{2}(\nabla\mathbf{u} + \nabla\mathbf{u}^\top)$. In addition, E and ν are the Young's modulus and Poisson ratio of the ECM while μ_1 and μ_2 denote its shear and bulk viscosity, respectively.

2.5. *General comments concerning the model*

We firstly remark that throughout the rest of the paper the external forces $\mathbf{f}_{\text{ext}}$ are assumed to be zero. This differs from numerous previous studies, which have incorporated a restoring body force which depends on the ECM displacement (Murray, 1989) or velocity (Manoussaki et al., 1996; Manoussaki, 2003). This has been motivated by the premise that the ECM is attached to an underlying substrate which restrains its movement, with a resultant displacement dependent force constraining the ECM. However, this restricts the modelling to specific, and relatively uncommon, "substrate-on-substrate" scenarios which we do not consider; thus, any such body force is neglected.

Secondly, nonlocal effects for diffusion, haptotaxis and forces have been considered, based on the generic idea that the area of influence (cell forces) or sensing (cell diffusion and haptotaxis) does not reduce to a single point for a cell. This is especially motivated by the current absence of a comparative study of how each nonlocal phenomenon influences the emergence of pattern.

Moreover, for simplicity, cell-cell interactions have not considered, although it is known that intracellular communication across gap junctions play a role in cell behaviour. This feature has been contemplated in other theoretical works (see, for example Ramtani, 2004).

Finally, we note that other authors additionally include nonlocal terms in the mechanical constitutive equation of the ECM, on the grounds that the ECM is usually a fibrous material and fibres have the ability to transmit stress between distant points (Cruywagen et al., 1997; Namy et al., 2004; Murray, 1989). However, huge efforts have devoted in recent years to the modelling of anisotropic fibrous biological tissues (see Alastrué et al., 2007; Peña et al., 2007 and references therein), showing that simple local models are perfectly capable of reproducing the required mechanical behaviour. Hence, no long range effects were considered in expression (14) for the ECM stress.

To simplify the subsequent analysis and to assess the relative importance of the various effects, we non-dimensionalise and reorganise the equations of the model (see the Appendix for details). For notational simplicity, we drop the asterisks that indicate the

nondimensional parameters and variables for the rest of the article. In doing so, the non-dimensional version of the system becomes

$$\frac{\partial n}{\partial t} + \nabla \cdot \left[-\left(D_1 - \frac{M p_{\text{cell}}}{(1+\lambda n^2)^2}\left(1 - \lambda n^2 - 2\lambda\beta n \nabla^2 n\right)\right)\nabla n + \left(D_2 + \frac{M\beta p_{\text{cell}}}{1+\lambda n^2}\right)\nabla\left(\nabla^2 n\right) + h_1 n \nabla\rho - h_2 n \nabla\left(\nabla^2\rho\right) + n\frac{\partial \mathbf{u}}{\partial t} + M\frac{n+\beta\nabla^2 n}{1+\lambda n^2}\nabla p_{\text{cell}}\right] = rn(1-n), \tag{15}$$

$$\frac{\partial \rho}{\partial t} + \nabla \cdot \left[\rho \frac{\partial \mathbf{u}}{\partial t}\right] = 0, \tag{16}$$

$$\nabla \cdot \left[\boldsymbol{\varepsilon} + \bar{\nu}\theta \mathbf{I} + \mu_1 \frac{\partial \boldsymbol{\varepsilon}}{\partial t} + \mu_2 \frac{\partial \theta}{\partial t}\mathbf{I} + p_{\text{cell}}\frac{n+\beta\nabla^2 n}{1+\lambda n^2}\mathbf{I}\right] = \mathbf{0}, \tag{17}$$

where $\bar{\nu} = \nu(1-2\nu)^{-1} > 0$.

3. Linear stability analysis

The system of Eqs. (15)–(17) has three sets of homogeneous steady state solutions:

$$\begin{aligned} &n^* = \rho^* = 0, \quad \mathbf{u}^* = \mathbf{0}; \qquad n^* = 1, \quad \rho^* = 0, \quad \mathbf{u}^* = \mathbf{0}; \\ &n^* = \rho^* = 1, \quad \mathbf{u}^* = \mathbf{0}. \end{aligned} \tag{18}$$

Here, the asterisk denotes the homogeneous steady state; it should be clear from context when an asterisk refers to the steady state or, as in the Appendix, is used to explicitly label a non-dimensional parameter of variable. The first two solutions are not relevant from a biological perspective, since $\rho = 0$; thus, we perform a linear stability analysis (Maini et al., 1991) around the third homogeneous steady state.

For this purpose, we first linearise the system around the steady state of interest to obtain the following system, where now $(n, \rho, \mathbf{u})$ denote variations from the steady state

$$\frac{\partial n}{\partial t} - (D_1 - M p_0 \tau_2)\nabla^2 n + (D_2 + M p_0 \beta \tau_1)\nabla^4 n + h_1 \nabla^2 \rho - h_2 \nabla^4 \rho + \frac{\partial \theta}{\partial t} + M\tau_1 K_{\text{eff}}^0 \nabla^2 \theta + r_0 n = 0, \tag{19}$$

$$\frac{\partial \rho}{\partial t} + \frac{\partial \theta}{\partial t} = 0, \tag{20}$$

$$\frac{1}{2}\mu_1 \nabla \cdot \left[\frac{\partial}{\partial t}\left(\nabla \mathbf{u} + \nabla^\top \mathbf{u}\right)\right] + \mu_2 \nabla\left[\frac{\partial}{\partial t}(\nabla \cdot \mathbf{u})\right] + \frac{1}{2}\nabla \cdot \left[\nabla \mathbf{u} + \nabla^\top \mathbf{u}\right] + \bar{\nu}\nabla(\nabla \cdot \mathbf{u}) + p_0\tau_2 \nabla n + K_{\text{eff}}^0 \tau_1 \nabla(\nabla \cdot \mathbf{u}) + \beta p_0 \tau_1 \nabla\left(\nabla^2 n\right) = \mathbf{0}, \tag{21}$$

where $\tau_1 \stackrel{\text{def}}{=} (1+\lambda)^{-1} > 0$, $\tau_2 \stackrel{\text{def}}{=} (1-\lambda)(1+\lambda)^{-2}$, $p_0 \stackrel{\text{def}}{=} p_{\text{cell}}(0)$, $r_0 \stackrel{\text{def}}{=} r(0)$ and $K_{\text{eff}}^0 \stackrel{\text{def}}{=} K_{\text{pas}} - p_0/\theta_1 > 0$. Observe that for high values of the cell stress saturation $\lambda > 1$, and thus $\tau_2 < 0$. When $\tau_2 > 0$, we will additionally require that

$$p_0 < p_0^{\max} = \frac{D_1}{M\tau_2} \tag{22}$$

so that the effective short range diffusion coefficient in Eq. (19) always takes positive values and the problem is well posed. Note that this is not a severe restriction, since $p_0^{\max}$ is high compared to the range of physiological values of p_0.

We first investigate if the steady state $(n^*, \rho^*, \mathbf{u}^*) = (1, 1, \mathbf{0})$ is stable under a homogeneous perturbation. We are therefore interested in perturbations of the form $(n, \rho, \mathbf{u}) = (N(t), R(t), \mathbf{U}(t))$. Note that given that the perturbation does not have any spatial dependence, the associated strain will be zero, in particular, $\theta = 0$. Furthermore, we will assume that any rigid body movement is prevented by means of the imposition of adequate boundary conditions. Under these conditions, the growth of spatially homogeneous perturbations of the displacement $\mathbf{u}$ from the steady state is not permitted. Regarding n and ρ, substitution in Eqs. (19) and (20) yields

$$\begin{aligned} &\frac{dN}{dt} + r_0 N = 0, \\ &\frac{dR}{dt} = 0 \end{aligned} \tag{23}$$

with trivial solutions

$$\begin{aligned} &N(t) = N|_{t=0} e^{-r_0 t}, \\ &R(t) = \text{const.} \end{aligned} \tag{24}$$

Clearly, homogeneous perturbations around the steady state of interest do not grow in time and the steady state is (Lyapunov) stable.

Next, in the case of pattern formation, we are interested in the conditions that must hold for the steady state to be unstable to *spatial* disturbances. This is why we now look for solutions of the linearised system in the form

$$(n, \rho, \mathbf{u}) \propto e^{\sigma t + i\mathbf{k}\cdot\mathbf{r}}, \tag{25}$$

where σ is the eigenvalue which determines temporal growth of spatial perturbations around the steady state of wave number $\mathbf{k} = (k_x, k_y, k_z)$ and $\mathbf{r} = (x, y, z)$ denotes the position vector.

If we substitute (25) in (19)–(21) and require the solution to be non-trivial, we obtain the following equation for σ:

$$\sigma k^2 \left[\frac{1}{2}k^2(1+\mu_1\sigma)\right]^2 \left[\mu\sigma^2 + b\big(k^2\big)\sigma + c\big(k^2\big)\right] = 0, \tag{26}$$

where $k = |\mathbf{k}|$, $\mu = \mu_1 + \mu_2$ and $b(k^2)$ and $c(k^2)$ are polynomials of order two and three in k^2, respectively, with the following expressions:

$$b(k^2) = \left[\gamma + \mu r_0 - p_0\left(\tau_2 + \tau_1\theta_1^{-1}\right)\right] + \left[\mu(D_1 - Mp_0\tau_2) + \beta p_0\tau_1\right]k^2 + \mu[D_2 + Mp_0\beta\tau_1]k^4. \tag{27}$$

$$c(k^2) = \left[r_0\gamma - p_0 r_0\tau_1\theta_1^{-1}\right] + \left[D_1\gamma - p_0\left(D_1\tau_1\theta_1^{-1} + \tau_2\widetilde{h}_1\right)\right]k^2 + \left[D_2\gamma - p_0\left(D_2\tau_1\theta_1^{-1} + \tau_2 h_2 - \beta\tau_1\widetilde{h}_1\right)\right]k^4 + \beta h_2 p_0\tau_1 k^6, \tag{28}$$

where $\gamma = 1 + \bar{\nu} + K_{\text{pas}}\tau_1$ and $\widetilde{h}_1 = h_1 + M(1 + \bar{\nu})$.

All the solutions of Eq. (26) with $\sigma > 0$ for some $k^2 > 0$ are unstable to spatial disturbances and will grow exponentially in time, leading to spatially structured solutions typical of biological patterns. In practice, these solutions will not grow indefinitely, due to several non-linear terms that have been necessarily neglected in the linear stability analysis: the quadratic term in the logistic growth for the cell concentration, the saturation of the cellular stress given by the term λn^2 and the disappearance of active stresses outside the strain range $\theta_1 < \theta < \theta_2$.

Trivial solutions of Eq. (26) are $\sigma = 0$ and $\sigma = -\mu_1^{-1}$, which we do not need to consider as they are non positive. The remaining solutions are the zeros of the quadratic polynomial in σ within the right-hand brackets of Eq. (26). In particular, we will focus on the solution with the largest real part, since it is the one that controls pattern growth and is given by

$$\sigma\left(k^2\right) = \frac{-b(k^2) + \sqrt{b^2(k^2) - 4\mu c(k^2)}}{2\mu}. \tag{29}$$

Expression (29) is denoted as the dispersion relation (Murray, 1989) and provides valuable information since it immediately shows whether pattern can develop and, if so, the range of wavelengths k and spatial periodicity of emerging patterns (see Fig. 1).

In our model, $b(k^2)$ cannot take negative values since all the coefficients are positive.[1] Given $b(k^2) > 0$, a necessary and sufficient condition to ensure that Re $\sigma(k^2) > 0$ for some $k^2 > 0$ is $c(k^2) < 0$.

Considering $c(k^2)$ in detail, note the coefficients of k^2 and k^4 can be negative, so a range of wave numbers in which c takes negative values, and hence σ is positive can exist (Fig. 1b). Note that in this range of instability the imaginary part is always zero, so the bifurcation is indeed a Turing bifurcation; Hopf and wave bifurcations are not possible with our model, as required for stable biological pattern.

It is important to remark that, given the positivity of the highest order coefficient in $c(k^2)$, we have $c(k^2) > 0$ for sufficiently large k^2, and hence the corresponding modes are stable. In other words, spatial patterns with arbitrarily high wave number—with wavelength that tends to zero—cannot grow. Apart from an absence of at least one of the non-local terms, the dispersion relation will always show that, in the case of pattern, there is only a finite window of wavelengths that can grow. From our perspective, this is the only

[1] The term $\tau_2 + \tau_1\theta_1^{-1}$ is negative for positive values of λ provided that θ_1 lies within the range $-1 < \theta_1 < 0$, that is, the whole range of physical validity, since θ_1 is a compressive volumetric strain and must be larger than -1 to ensure that the volume remains positive locally. With this remark, the demonstration that $b(k^2) > 0$ is trivial.

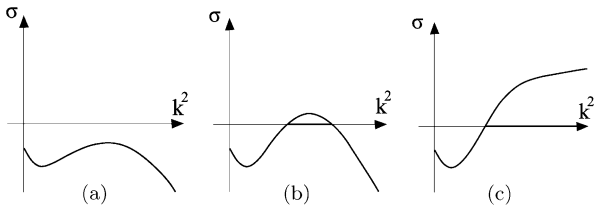

Fig. 1 Qualitative dispersion relations: (a) The whole range of wave numbers is stable, so no spatial pattern can emerge; (b) Finite range of unstable modes; (c) Unbounded range of unstable modes. Only situations (a) and (b) are possible with our model, except for degeneracy in the non-local cellular interactions.

legitimate option with a continuum model. It has been claimed elsewhere (Murray, 1989; Manoussaki et al., 1996) that dispersion relations possessing positive growth rates at large wave numbers (Fig. 1c) are also valid, with the ultimate spatial structure depending intimately on the initial conditions.

Here, however, we have found by means of numerical simulations (see Section 5) that rather than a critical dependence on the initial conditions, the outcome of models with dispersion relations such as in Fig. 1c is a spatial pattern with a pathological dependence on the mesh size irrespective of the initial conditions; the prevailing pattern always being the one corresponding to the smallest wavelength that the spatial discretisation is able to reproduce. The physical interpretation of a dispersion relation with unstable modes at arbitrarily large wave number is pattern formation with an arbitrarily small wavelength, eventually approximating the cellular-level scale. On approaching this scale of patterning any continuum model reaches its limit of validity and must be replaced by a discrete version to confirm the formation and stability of such fine grained pattern.

In the following, we shall derive analytical bifurcation conditions for the full model and special cases where one of the three long range effects is neglected. We have taken as bifurcation parameters the cellular stress p_0 and the effective haptotaxis coefficient $\widetilde{h}_1$.

3.1. Bifurcation conditions for the general case

A necessary and sufficient condition for the appearance of finite wavelength pattern is that $c(q) = a_0 + a_1 q + a_2 q^2 + a_3 q^3$ takes negative values for a finite range of q, where $q = k^2 \geq 0$ and a_n is the coefficient of k^{2n} in Eq. (28). Note that $a_0 > 0$ and $a_3 \geq 0$.

3.1.1. Bifurcation conditions when $a_3 > 0$, $a_2 \neq 0$

We initially work with $a_3 > 0$, $a_2 \neq 0$. Let $q_\pm$ be the turning points of $c(q)$, given by the roots of $a_1 + 2a_2 q_\pm + 3a_3 q_\pm^2 = 0$. Assuming their existence, they are given by $q_\pm = (-a_2 \pm \sqrt{a_2^2 - 3a_1 a_3})/3a_3$. For an instability region, we require:

I q_+ exists and is real
II $q_+ > 0$
III $c(q_+) < 0$

We initially consider constraints [I] and [II] above. With $a_3 > 0$, $a_2 \neq 0$, it is straightforward to deduce that these yield

$$\text{either} \quad a_2 > 0,\ a_1 < 0 \quad \text{or} \quad a_2 < 0,\ 3a_3 a_1 / a_2^2 < 1. \tag{30}$$

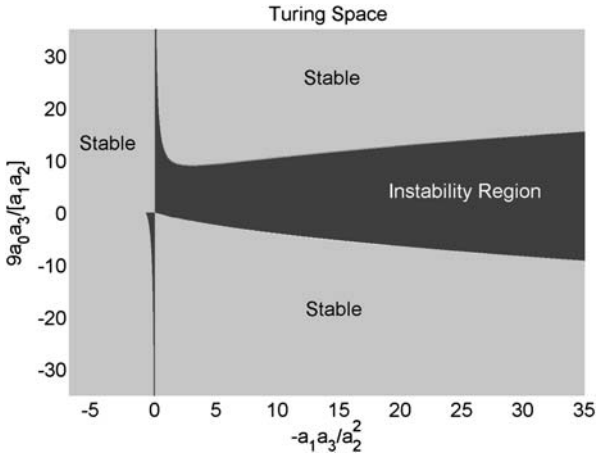

Fig. 2 The Turing space, that is the region of parameter space where a Turing instability is possible, when $a_2, a_3 \neq 0$ assuming an appropriate selection of wavenumber and domain size.

By repeatedly using the fact $a_1 + 2a_2q_+ + 3a_3q_+^2 = 0$, constraint [III] can be written as

$$0 > \frac{27a_3^2}{|a_2|^3}c(q_+) = \frac{27a_3^2}{|a_2|^3}\left\{\left(a_0 - \frac{a_1a_2}{9a_3}\right) - \frac{2}{27}\frac{a_2^3}{a_3^2}(1+y)\left(-1+\sigma\sqrt{1+y}\right)\right\}$$

$$\Rightarrow \quad 0 > \sigma y\left(1 - \frac{2(1+y)}{1+\sigma\sqrt{1+y}} - s\right), \tag{31}$$

where $y = -3a_1a_3/a_2^2$, $s = 9a_0a_3/[a_1a_2]$ and $\sigma = \text{sign}(a_2) = -\text{sign}(ys)$. Noting $\text{sign}(a_1) = -\text{sign}(y)$, the instability Turing space, as given by (30) and (31), is determined solely in terms of the two parameter groupings, y and s enabling the depiction of the Turing space in Fig. 2.

While the Turing space for mechanochemical models is often considered to depend on too many parameter groupings for its algebraic or graphical description to be useful (Murray, 1989) this is not the case for the current model. The graphical representation of the Turing space in a low dimensional space presented in Fig. 2, which is universally valid unless there is a degeneracy in a_2 or a_3, allows one to readily deduce how parameter changes affect stability. For example, given $a_1 < 0$, suppose D_2 or γ is increased. This increases a_2 and thus reduces $y = -3a_1a_3/a_2^2 > 0$ while $s = 9a_0a_3/[a_1a_2]$ increases, regardless of the sign of a_2. Thus, motion in the (y, s) Turing space depicted in Fig. 2 is from the lower right to the upper left in the half plane $y > 0$. Depending on parameter values one can see therefore that increasing D_2 or γ can move one from a region of stability to instability and vice-versa according to parameter values. In contrast, sufficient increases in r_0 for instance, will always eventually drive the system to stability.

3.1.2. Bifurcation conditions when $a_3 = 0$

This situation is of particular interest since it encompasses the case where $\beta h_2 = 0$, that is, when long-range haptotaxis and/or cell forces are identically zero.

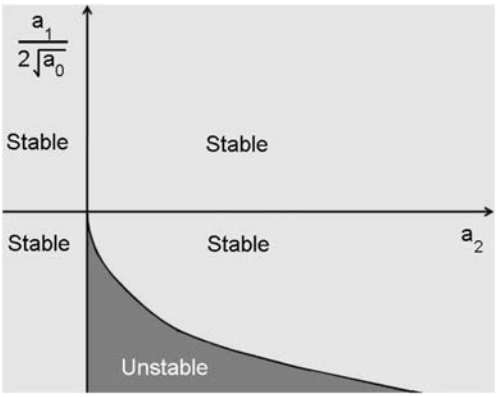

Fig. 3 The Turing space, that is the region of parameter space where a Turing instability is possible, when $a_3 = 0$ assuming an appropriate selection of wave number and domain size.

Now $c(q) = a_0 + a_1 q + a_2 q^2$, with $a_0 > 0$. We have to require that the coefficient of the largest power of q, i.e. a_2, is positive, to ensure that the range of unstable modes is finite and to prevent the possibility of a dispersion relation with positive growth rates at arbitrarily large wavenumbers. With this additional constraint in place, one can take limits of the conditions (31), or consider an explicit calculation, to show that the instability is given by

$$a_1 < 0, \qquad a_2 > 0, \qquad a_1^2 > 4a_0 a_2 \tag{32}$$

which again can be readily depicted in terms of two parameter groupings, as shown in Fig. 3. We will return to possibility of positive growth rates at arbitrarily large numbers below.

3.1.3. Bifurcation conditions when $a_2 = 0, a_3 > 0$

For $a_2 = 0$, one requires a perfect parameter fine-tuning which is therefore not highly relevant biologically; one also requires that $a_3 > 0$ to prevent positive growth rates at arbitrarily large wavenumbers. For completeness, we record the instability conditions, which are

$$a_1 < 0, \qquad \frac{27}{4} a_0^2 a_3 < |a_1|^3 \tag{33}$$

which is also consistent with taking limits of Eq. (31) when $a_1 < 0$.

3.2. A detailed study of bifurcation conditions in special cases

Interpreting conditions (30) and (31) in terms of biophysical interactions is typically not an easy task in the general case. Special cases are also of enormous interest and allow further insight and will be considered below.

3.2.1. Bifurcation conditions for the case $a_2 \neq 0$, $a_3 \ll 1$, $|y| \ll 1$

The case $|y| \ll 1$, $a_3 \ll 1$ is of considerable interest and will typically occur for weak non-local effects if either non-local haptotatic effects or the non-local effects of cell density on the stress $\boldsymbol{\sigma}_{\text{cell}}$ are smaller than the dominant, albeit weak, non-local effect. For this purpose, we can use a Taylor expansion of the condition (31), distinguishing between the case $a_2 > 0$ and $a_2 < 0$.

In the case $a_2 < 0$, inequality (31) reduces to $27a_3^2a_0 < 4|a_2|^3$, which always holds for sufficiently small values of a_3. Hence, if $a_2 < 0$ and $|y| \ll 1$, an instability region exists. However, note that on taking the limit $a_3 \to 0$ the larger coefficient of $c(q)$ would then be negative, indicating that the instability would degenerate in pattern at arbitrarily small wavelength. Therefore, this combination of parameters, $a_2 < 0$ and $|y| \ll 1$, would yield a fine grained pattern that cannot be modelled in the continuum approximation.

Therefore, we are interested in the case $a_2 > 0$. In this case, a Taylor expansion of (31) for y shows that, providing $|y| \ll 1$ and given $a_3 \geq 0$, one has the inequalities

$$a_1 < 0, \qquad a_2 > 0, \qquad 1 > \frac{4a_0a_2}{a_1^2} \tag{34}$$

for an instability region, which are much simpler than the conditions in the general case and permit a more detailed analysis. Again, these conditions are depicted in Fig. 3.

As in the general case, it is possible to reformulate conditions (34) in terms of only two parameter groupings, noticeably simplifying the analysis. These are $\widetilde{h}_1$ and $\widetilde{x}$, the last of which is defined as

$$\widetilde{x} \stackrel{\text{def}}{=} \frac{D_1\gamma}{\tau_2}\frac{1}{p_0} + \frac{D_1\tau_1}{|\theta_1|\tau_2}.$$

Conditions (34) are fulfilled if and only if both $\tau_2 > 0$ and the following set of restrictions is imposed on $\widetilde{x}$, $\widetilde{h}_1$ (see Figs. 4a–c):

(a) $\widetilde{x} < \widetilde{h}_1$
(b) $\widetilde{x} > \phi - \psi\widetilde{h}_1$
(c) $(\widetilde{x} - \widetilde{h}_1)^2 > \alpha\widetilde{x}(\widetilde{x} - \phi + \psi\widetilde{h}_1)$

where α, ψ and ϕ are nonnegative parameters, which do not depend on $\widetilde{x}$ or $\widetilde{h}_1$, with expressions

$$\alpha \stackrel{\text{def}}{=} 4r_0D_2/D_1^2, \qquad \psi \stackrel{\text{def}}{=} \beta\tau_1D_1/[\tau_2D_2], \qquad \phi \stackrel{\text{def}}{=} h_2D_1/D_2.$$

Thus, the Turing space in the $(\widetilde{x}, \widetilde{h}_1)$ plane, and hence in the $(p_0, \widetilde{h}_1)$ plane, is delimited by three curves. In the $(\widetilde{x}, \widetilde{h}_1)$ plane, two of these delimiting curves are straight lines. The third is a hyperbola. One can therefore immediately determine how the overall system's stability properties are altered on changing parameters by simply considering the region within the positive quadrant which is delimited by two straight lines and a hyperbola (see Fig. 5). It can be proved that the three curves intersect at a single point P with coordinates $(\phi(1+\psi)^{-1}, \phi(1+\psi)^{-1})$, which is additionally the point at which the straight line given by condition (b) is tangent to the hyperbola.

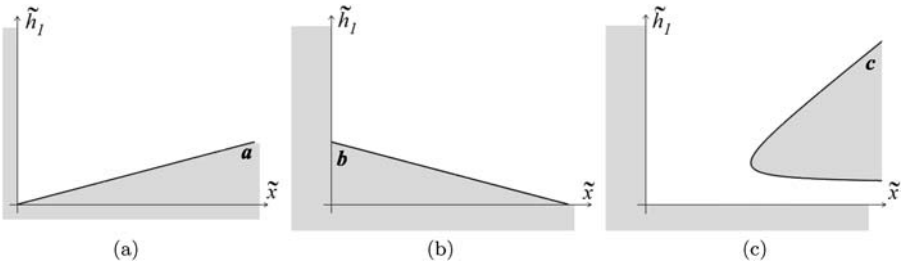

Fig. 4 Conditions on $\widetilde{x}$, $\widetilde{h}_1$ for the appearance of spatial pattern in the case $a_2 \neq 0$, $a_3 \ll 1$, $y \ll 1$: (a) $\widetilde{x} < \widetilde{h}_1$, (b) $\widetilde{x} > \phi - \psi\widetilde{h}_1$, (c) $(\widetilde{x} - \widetilde{h}_1)^2 > \alpha\widetilde{x}(\widetilde{x} - \phi + \psi\widetilde{h}_1)$. Shaded areas are excluded by the constraint in question or the fact $\widetilde{x}, \widetilde{h}_1 > 0$ (which always holds given that $\tau_2 > 0$).

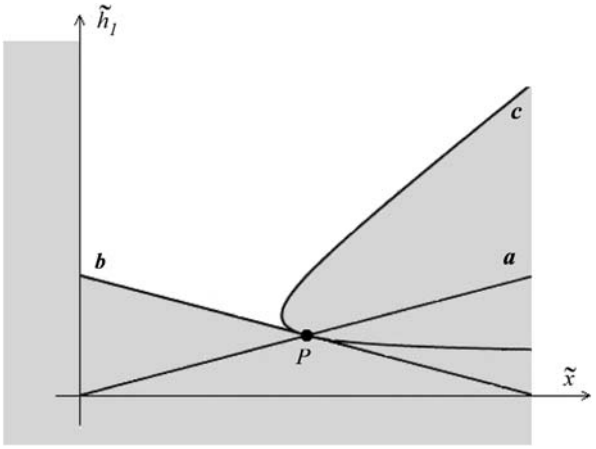

Fig. 5 Global representation of the necessary and sufficient conditions for the appearance of pattern in the case $a_2 \neq 0$, $a_3 \ll 1$, $y \ll 1$. Shaded areas are excluded, i.e. correspond to regions of stability where pattern does not emerge.

3.2.2. Bifurcation conditions when $a_3 = 0$

We revisit this situation, which is also of particular interest since it allows the study of the case $\beta h_2 = 0$, which implies the long-range haptotaxis and/or cell forces are identically zero. In the following, we examine conditions (32) in detail for two different cases: $h_2 = 0$ and $\beta = 0$.

3.2.3. No long range haptotaxis: $D_2, \beta > 0$, $h_2 = 0$

In this situation, $\phi = 0$ and necessary and sufficient conditions for pattern formation are $\tau_2 > 0$ together with the following restrictions on $\widetilde{x}$, $\widetilde{h}_1$ (see Fig. 6):

(a) $\widetilde{x} < \widetilde{h}_1$
(b) $\widetilde{h}_1 > -\widetilde{x}/\psi$
(c) $(\widetilde{x} - \widetilde{h}_1)^2 > \alpha\widetilde{x}(\widetilde{x} + \psi\widetilde{h}_1)$

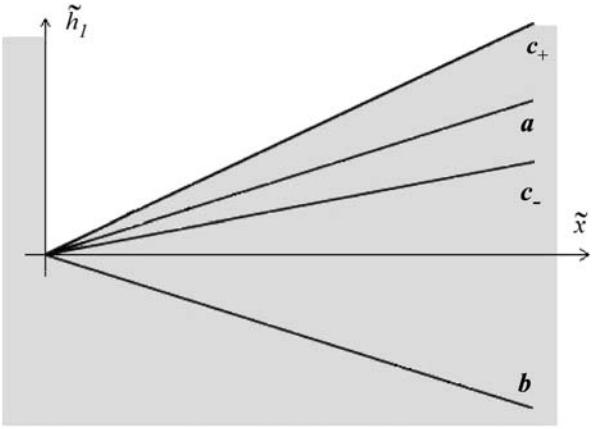

Fig. 6 Global representation of the necessary and sufficient conditions for the appearance of pattern in the case D_2, $\beta > 0$, $h_2 = 0$. Shaded areas are excluded, i.e. correspond to regions of stability where pattern does not emerge.

This case is degenerate compared to the previous, since the delimiting curve of condition (c) no longer corresponds to a hyperbola, but instead to a pair of straight lines $\widetilde{h}_1^{\pm}$ given by:

$$\widetilde{h}_1^{\pm} = \left(1 + \frac{\alpha\psi}{2} \pm \sqrt{\left(1 + \frac{\alpha\psi}{2}\right)^2 + (\alpha - 1)}\right)\widetilde{x} \tag{35}$$

with slopes $\partial\widetilde{h}_1^{+}/\partial\widetilde{x} > 1$ and $\partial\widetilde{h}_1^{-}/\partial\widetilde{x} < 1$.

Thus, all the delimiting curves of conditions (a)–(c) are straight lines in the $(\widetilde{x}, \widetilde{h}_1)$ plane going through the origin.

It should be noticed that in this particular case a_2 is always positive, irrespective of the value of any model parameter, so the possibility of having diverging growth rates of unstable modes at large wavenumbers is ruled out.

3.2.4. No long range cellular forces: D_2, $h_2 > 0$, $\beta = 0$

In this situation $\psi = 0$ and, in addition to requiring $\tau_2 > 0$, the following set of restrictions must be imposed on $\widetilde{x}$, $\widetilde{h}_1$ to drive the system to instability (see Fig. 7):

(a) $\widetilde{x} < \widetilde{h}_1$
(b) $\widetilde{x} > \phi$
(c) $(\widetilde{x} - \widetilde{h}_1)^2 > \alpha\widetilde{x}(\widetilde{x} - \phi)$

As in the case $a_3 \ll 1$, $|y| \ll 1$, the Turing space in the $(\widetilde{x}, \widetilde{h}_1)$ plane is delimited by two straight lines and a hyperbola. These intersect at point P of coordinates (ϕ, ϕ), where the vertical line delimiting condition (b) is tangent to the hyperbola.

It should be noted that the highest order coefficient of $c(k^2)$ is a_2, which in this specific case can be negative if the model parameters are suitably chosen, leading to a scenario

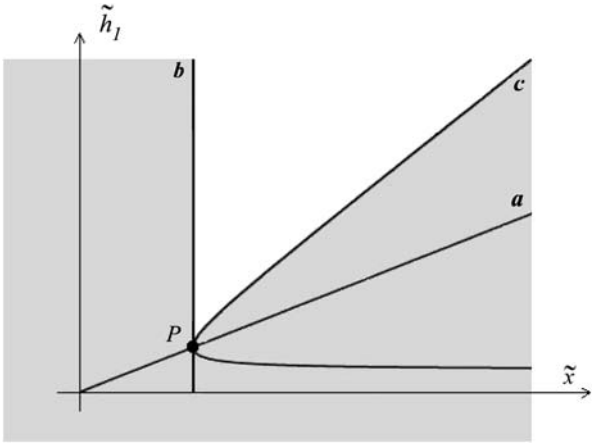

Fig. 7 Global representation of the necessary and sufficient conditions for the appearance of pattern in the case D_2, $h_2 > 0$, $\beta = 0$. Shaded areas are excluded, i.e. correspond to regions of stability where pattern does not emerge.

with an infinite range of unstable wavenumbers. In particular, we have

$$a_2 < 0 \quad \Leftrightarrow \quad \tau_2 > 0, \quad h_2 > h_2^*, \quad p_0 > \frac{D_2\gamma}{\tau_2(h_2 - h_2^*)} \tag{36}$$

with $h_2^* \stackrel{\text{def}}{=} D_2\tau_1/[\tau_2|\theta_1|]$.

Due to the reasons expressed above, if the appearance of pattern at arbitrarily small wavelength is deemed undesirable, the above combination of model parameters should be avoided from the outset.

3.3. The influence of model parameters

3.3.1. The influence of model parameters in the general setting

When conditions (30), (31) are satisfied for $a_2 \neq 0$, $a_3 > 0$, or conditions (32) are satisfied for $a_3 = 0$, or conditions (33) are satisfied for $a_2 = 0$, there is a finite range of linearly unstable wavenumbers $k_1^2 < k^2 < k_2^2$ in which $c(k^2) < 0 \Leftrightarrow \mathrm{Re}\,\sigma(k^2) > 0$. However, note that in a finite-length domain the possible wavenumbers of allowable patterns are discrete and depend in part on the boundary conditions. Hence, the appearance of pattern also requires there is at least one wavenumber of the allowed range which is unstable. Finite domains put therefore considerable restrictions on the permissible patterns; in particular, the model is always stable on a sufficiently small domain.

Interestingly, it is possible to analytically show that the system is always stable when $\bar{\nu}$ is sufficiently large. In this case, $a_2 \simeq D_2\bar{\nu} + \beta\tau_1 M p_0\bar{\nu} > 0$ and $a_1 \simeq D_1\bar{\nu} - \tau_2 M p_0\bar{\nu}$, which is also positive provided that (22) holds. Since a_0 is positive and a_3 is non-negative, we have that, for sufficient large values of $\bar{\nu}$, $c(q) \geq c(0) = a_0 > 0$ for all $q > 0$, so the system is stable.

Similarly, given $\tau_2 > 0$, then sufficiently increasing the coefficient of haptotaxis, h_1, or the effective haptotaxis coefficient $\widetilde{h}_1$, while keeping other model parameters fixed will

result in the instability conditions being satisfied. In this sense, we have the modelling prediction that haptotaxis tends to invoke pattern formation.

Finally, if $\tau_2 p_0$ is negative, or if it is positive and sufficiently small so that $a_1, a_2 > 0$ then the system is stable. Noting that $p_0 > 0$ we have thus demonstrated, in a general setting, that one requires both $\tau_2 > 0$ and p_0 to surpass a critical lower bound for patterning to take place.

3.3.2. The influence of model parameters: special cases

The expression of the analytical instability conditions in terms of two parameter groupings allows the visualisation of the Turing space in the $(\widetilde{x}, \widetilde{h}_1)$ plane, enabling an easier interpretation in terms of biophysical mechanisms. In this plane, the limiting curves are two straight lines and a hyperbola, so the analysis of the instability region is immediate. Changing other model parameters shifts the curves but, as long as signs are maintained ($D_1 > 0$, $D_2 > 0$, etc.), this does not change the qualitative details of when the system is stable or unstable.

Such analyses are illustrated by, but not restricted to, the following:

- A general condition for instability is $\tau_2 > 0$, which limits the extent of cell stress saturation. As $\tau_2 \to 0$ ($\psi \to \infty$), with $\widetilde{h}_1$ fixed, we have that the Turing space shrinks to zero as the lower bound on p_0 for patterning tends to infinity.
- For the dispersion relation to predict wavenumbers with positive growth, it is sufficient to require firstly that $\tau_2 > 0$, secondly that $\psi = \beta\tau_1 D_1/[\tau_2 D_2] > 0$ and finally that both the effective haptotaxis coefficient $\widetilde{h}_1$ and the cell force p_0 exceed critical lower bounds.
- When $\beta = 0$ with $D_2,\ h_2 > 0$, there is a singular behaviour in that there is upper bound on p_0 whenever $\widetilde{h}_1 > \phi$, i.e. the effective haptotaxis coefficient is sufficiently large.
- For $\beta, \tau_2 > 0$, the constraint

$$\widetilde{h}_1 > \max\left(\frac{h_2\tau_2}{\beta\tau_1} - \frac{\widetilde{x}}{\psi},\ \widetilde{x}\left[1 + \frac{\alpha\psi}{2} + \frac{1}{2}\sqrt{\alpha^2\psi^2 + 4\alpha(1+\psi)}\right]\right) \tag{37}$$

  is sufficient to ensure one is in the instability region.

4. Finite element formulation

In this section, we shall illustrate the derivation of a finite element formulation for the numerical solution of Eqs. (1)–(10). The non-local terms within the system of equations are fourth order, which requires special attention. The standard spatial discretisation of the equations would require C^1 continuity, yielding finite element interpolations that are complicated to build. The use of C^1 conforming interpolation schemes for such problems is being superseded increasingly by formulations that require only C^0 continuity (see, for example Barrett et al., 1999; Feng and Prohl, 2003 for the Cahn–Hilliard equation).

In this work, we use a mixed finite element method, which decomposes the model partial differential equations, as defined by Eqs. (1)–(3), into a system of five equations with no fourth-order terms, allowing a C^0 spatial interpolation. Thus, we introduce two auxiliary variables $\kappa = \nabla^2 n$ and $\varphi = \nabla^2 \rho$ and consider the primary unknowns to be the

cell concentration n, the ECM density ρ, the ECM displacement $\mathbf{u}$ and the new pair of variables κ and φ. Equations (1)–(3) can be replaced by the following system:

$$\frac{\partial n}{\partial t} + \nabla \cdot \left[-D_1 \nabla n + D_2 \nabla \kappa + h_1 n \nabla \rho - h_2 n \nabla \varphi + n \frac{\partial \mathbf{u}}{\partial t} + M \nabla \cdot \boldsymbol{\sigma}_{\text{cell}} \right] = r(\theta) n \left(1 - \frac{n}{N} \right), \tag{38}$$

$$\frac{\partial \rho}{\partial t} + \nabla \cdot \left[\rho \frac{\partial \mathbf{u}}{\partial t} \right] = 0, \tag{39}$$

$$\nabla \cdot \left[\frac{E}{1+\nu} \left(\boldsymbol{\varepsilon} + \frac{\nu}{1-2\nu} \theta \mathbf{I} \right) + \mu_1 \frac{\partial \boldsymbol{\varepsilon}}{\partial t} + \mu_2 \frac{\partial \theta}{\partial t} \mathbf{I} + p_{\text{cell}}(\theta) \frac{c + \beta \kappa}{1 + \lambda n^2} \mathbf{I} \right] = \mathbf{0}, \tag{40}$$

$$\kappa = \nabla^2 n, \tag{41}$$

$$\varphi = \nabla^2 \rho. \tag{42}$$

Then, we consider the function spaces associated with the finite element spatial discretisation:

$$\begin{aligned}
S^h &= \left\{ n^h \middle| n^h \in H^1(\Omega), n^h \in P^k(\Omega_e)\ \forall e, n^h = g \text{ on } \Gamma_g \right\}, \\
V^h &= \left\{ \delta n^h \middle| \delta n^h \in H^1(\Omega), \delta n^h \in P^k(\Omega_e)\ \forall e, \delta n^h = 0 \text{ on } \Gamma_g \right\}, \\
P^h &= \left\{ \kappa^h \middle| \kappa^h \in H^1(\Omega), \kappa^h \in P^k(\Omega_e)\ \forall e, \kappa^h = l \text{ on } \Gamma_l \right\}, \\
Q^h &= \left\{ \delta \kappa^h \middle| \delta \kappa^h \in H^1(\Omega), \delta \kappa^h \in P^k(\Omega_e)\ \forall e, \delta \kappa^h = 0 \text{ on } \Gamma_l \right\}, \\
U^h &= \left\{ \mathbf{u}^h \middle| u_i^h \in H^1(\Omega) \forall i, u_i^h \in P^k(\Omega_e)\ \forall i\ \forall e, \mathbf{u}^h = \mathbf{0} \text{ on } \Gamma \right\}, \\
R^h &= \left\{ \rho^h \middle| \rho^h \in H^1(\Omega), \rho^h \in P^k(\Omega_e)\ \forall e \right\}, \\
F^h &= \left\{ \varphi^h \middle| \varphi^h \in H^1(\Omega), \varphi^h \in P^k(\Omega_e)\ \forall e \right\}
\end{aligned}$$

with H^1 the Sobolev space of degree 1 and $P^k(\Omega_e)$ the space of the standard polynomial finite element shape functions on element Ω_e where k is the polynomial order. It has been assumed that the boundary conditions g and r can be represented exactly by the finite element basis. Note that due to the boundary conditions on ρ and $\mathbf{u}$, the space of trial functions is identical to the space of test (weighting) functions for $\mathbf{u}$ (U^h), ρ (R^h) and φ (F^h).

Following the standard procedure of integration by parts, and use of the boundary conditions, the weak (Galerkin) form of the problem reads:

Find $n^h \in S^h \times [0, T]$, $\kappa^h \in P^h$, $\rho^h \in R^h \times [0, T]$, $\varphi^h \in F^h$ and $\mathbf{u}^h \in U^h$ such that

$$\begin{aligned}
&\left(\delta n^h, n^h_{,t} \right)_\Omega + \left(\nabla \delta n^h, D_1 \nabla n^h - D_2 \nabla \kappa^h - h_1 n^h \nabla \rho^h \right. \\
&\qquad \left. + h_2 n^h \nabla \varphi^h - n^h \mathbf{u}^h_{,t} - M \nabla \cdot \boldsymbol{\sigma}^h_{\text{cell}} \right)_\Omega \\
&= -\left(\delta n^h, m \right)_{\Gamma_m} + \left(\delta n^h, r(\theta^h) n^h \left(1 - \frac{n^h}{N} \right) \right)_\Omega \quad \forall \delta n^h \in V^h,
\end{aligned} \tag{43}$$

$$\left(\delta\kappa^h, \kappa^h\right)_\Omega + \left(\nabla\delta\kappa^h, \nabla n^h\right)_\Omega = \left(\delta\kappa^h, q\right)_{\Gamma_q} \quad \forall\delta\kappa^h \in Q^h, \tag{44}$$

$$\left(\delta\rho^h, \rho^h_{,t}\right)_\Omega - \left(\nabla\delta\rho^h, \rho^h \mathbf{u}^h_{,t}\right)_\Omega = 0 \quad \forall\delta\rho^h \in R^h, \tag{45}$$

$$\left(\delta\varphi^h, \varphi^h\right)_\Omega + \left(\nabla\delta\varphi^h, \nabla\rho^h\right)_\Omega = \left(\delta\varphi^h, \nabla\rho^h \cdot \boldsymbol{\eta}\right)_\Gamma \quad \forall\delta\varphi^h \in F^h, \tag{46}$$

$$\left(\boldsymbol{\sigma}^h_{\text{cell}} + \boldsymbol{\sigma}^h_{\text{ecm}}, \frac{1}{2}\left(\nabla\delta\mathbf{u}^h + \nabla^\top\delta\mathbf{u}^h\right)\right)_\Omega = 0 \quad \forall\delta\mathbf{u}^h \in U^h, \tag{47}$$

$$\left(\delta n^h, n(\mathbf{x}, 0)\right)_\Omega = \left(\delta n^h, n_0(\mathbf{x})\right)_\Omega \quad \forall\delta n^h \in V^h, \tag{48}$$

$$\left(\delta\rho^h, \rho(\mathbf{x}, 0)\right)_\Omega = \left(\delta\rho^h, \rho_0(\mathbf{x})\right)_\Omega \quad \forall\delta\rho^h \in R^h, \tag{49}$$

where we have made repeated use of the standard notation for L_2-inner products:

$$(u, v)_\Psi = \int_\Psi uv \, \mathrm{d}\Psi \tag{50}$$

and, with a slight abuse of notation,

$$(\mathbf{u}, \mathbf{v})_\Psi = \int_\Psi \mathbf{u} : \mathbf{v} \, \mathrm{d}\Psi \tag{51}$$

for $\mathbf{u}$ and $\mathbf{v}$ denoting second order tensors.

Equations (43), (45), and (47) are discretised in time according to the generalised trapezoidal method (Hughes, 2000), which depends on a parameter ζ, taken to be in the interval [0, 1], such that for $\zeta = 0, 0.5, 1.0$ the forward Euler, Crank–Nicolson, and backward Euler integration methods are recovered, respectively.

Next, the semi-discrete system is discretised in space making use of the finite element method. Within this approach the domain Ω is discretised into n_{el} elements Ω^e, with $\Omega = \bigcup_{e=1}^{n_{el}} \Omega^e$. The primary unknown fields and their derivatives are thus interpolated within an element in terms of the nodal values through shape functions. Following a Bubnov–Galerkin approach, these same shape functions are also used for the interpolation of the test functions. The resultant nonlinear equations are consistently linearised allowing the use of a Newton–Raphson scheme to solve the system.

5. Numerical simulation

5.1. Description

Finite element simulations have been performed based on the above formulation, implemented in ABAQUS software (Dassault Systèmes Simulia Corp., 2006), with the aim of verifying the analytical conditions for pattern formation. In particular, we are interested in studying how the qualitative behaviour of the system depends on the instability interval of the dispersion relation and how the boundary conditions affect the emergence of pattern.

For definiteness, we consider a planar square domain and we have assumed the plane stress hypothesis for the mechanical behaviour of the ECM. Note that this example is relevant for any biological application where a cell population lies on a substrate and

has the potential to self-organise. One class of applications emerges from research investigating angiogenesis, which is the process of new blood vessel formation from pre-existing vessels via endothelial cell sprouting, proliferation, and migration (Conway et al., 2001). In particular, numerous *in vitro* models have been reported (Collen et al., 1998; Vailhé et al., 2001; Stéphanou et al., 2007) which reproduce the earlier phases of vascular growth, i.e. the formation of vascular cords. In such experimental models, endothelial cells are seeded on biogels such as collagen, fibrin, or matrigel. On fibrin gel, cells spontaneously self-organise by degrading the gel and by exerting traction forces which induce the formation of lacunae via the development of dilatation zones. Our simulation reproduces the conditions under which these experimental angiogenesis tests are performed. However, endothelial cells are not the only type of cells that generate pattern. For instance, in embryogenesis mesenchymal cells are thought to drive spatial pattern development, as exemplified by feather germ formation (Davidson, 1983a, 1983b).

5.1.1. Initial and boundary conditions

As initial conditions, we have considered that the substrate is undeformed, i.e. $\mathbf{u}(\mathbf{x}, 0) = 0$, and a uniform ECM density, $\rho(\mathbf{x}, 0) = 1\ \mathrm{gr/cm^3}$. The cell density, n, at the start of the simulation is a small random perturbation (5–15%) of the homogeneous steady state N.

As boundary conditions for $\mathbf{u}$, we have assumed that the displacement is restrained along the whole contour of the domain, i.e. $\mathbf{u} = 0$ on Γ.

With regard to the boundary conditions for n, several options exist, all of which can be suitable and biologically realistic, depending on the situation that one wants to model (see Murray, 1989). For example, an impermeable boundary can be modelled by means of a zero-flux boundary condition. Another biologically reasonable set of conditions is periodicity, which can be used in a two dimensional setting to simulate closed three dimensional boundaries. If the domain is surrounded by a hostile environment, Robin boundary conditions are an appropriate option: $\mathbf{J}_n \cdot \boldsymbol{\eta} = bn$, where the parameter b is a measure of the hostility. In a completely hostile exterior $b \to \infty$, so the boundary condition can be approximated by a simpler one of the Dirichlet type: $n = 0$. Finally, if we suppose that the environs is an infinite source of cells in which the cell concentration is approximately constant, an inhomogeneous Dirichlet boundary condition is also a valid choice.

Note that all the previous alternatives for the boundary conditions restrain the value of the cellular concentration n or the associated total flux $\mathbf{J}_n$. However, expressions (5) and (6), together with the fact that $\Gamma = \overline{\Gamma_q \cup \Gamma_l}$, where $\Gamma_q \cap \Gamma_l = \emptyset$, imply that, in order to have a well-posed problem, additional conditions must be additionally imposed at every point of the boundary on one the following derivatives of the cellular concentration: $\nabla n \cdot \boldsymbol{\eta}$ or $\nabla^2 n$. Unfortunately, the interpretation of these two possible boundary conditions in biological terms is not as straightforward. Clearly, the use of a fourth order model complicates the choice of appropriate boundary conditions.

To overcome this difficulty, in the numerical simulations we contemplate two different sets of boundary conditions:

– In Section 6.1, we have assumed that the boundary of the domain is impermeable for cells, thus setting $\mathbf{J}_n \cdot \boldsymbol{\eta} = 0$ on $\Gamma_m = \Gamma$ ($\Gamma_g = \emptyset$). As second boundary condition, we have tested two different options: $\nabla n \cdot \boldsymbol{\eta} = 0$ on $\Gamma_q = \Gamma$ ($\Gamma_l = \emptyset$) or $\nabla^2 n = 0$ on $\Gamma_l = \Gamma$ ($\Gamma_q = \emptyset$).
– In Section 6.2, we have replaced the zero-flux restriction by a Dirichlet boundary condition, setting $n = N$ on $\Gamma_g = \Gamma$ ($\Gamma_m = \emptyset$). Analogously to Section 6.1, the same two

options have been tested as the second boundary condition. As discussed before, this represents a situation where the environs effectively constitutes an infinite source of cells.

5.1.2. Model parameters estimation

Model parameters were obtained from the literature for fibroblasts, a type of mesenchymal cell routinely used in experimental works of cell migration:

- *Cell flux (short range)*: The short range diffusion coefficient D_1 was taken to be 1.7×10^{-10} cm^2/s from Barocas et al. (1995) and Shreiber et al. (2003). A value of 1.8×10^{-7} cell (Pa s)$^{-1}$ was prescribed for M, following previous work of the authors (Moreo et al., 2008). Briefly, M was fitted to reproduce the observed dependence of cell locomotion rate on the flexibility of the substrate (Pelham and Wang, 1997). Finally, it is quite difficult to find experimental data to fix the value of the short range haptotaxis coefficient h_1. Other theoretical studies have used values that vary in the range 10^{-8}–10^{-4} cm^2/s (gr/cm^3)$^{-1}$ (Dickinson and Tranquillo, 1993; Perumpanani and Byrne, 1999). In this work, a value of 10^{-4} cm^2/s (gr/cm^3)$^{-1}$ was used.
- *Cell kinetics*: The mean average doubling time for fibroblasts is 18–20 h (Ghosh et al., 2007), which yields a proliferation rate of $r_{\max} = 1$ day^{-1}. The parameter τ was taken to be 6×10^{-3} dyne/cell, so that observed changes (Ghosh et al., 2007) in the proliferation rate with substrate stiffness were reproduced. The mean projected area per fibroblast on a planar substrate is of the order of 10^3 μm^2 (Lo et al., 2000), so the maximum carrying capacity of the medium can be estimated to be 10^5 cell/cm^2.
- *Substrate mechanics*: The Young's modulus E and Poisson's coefficient ν were respectively chosen to be 10 kPa and 0.3, which are typical of substrate values used in cell migration experiments (Engler et al., 2004; Peyton and Putnam, 2005; Khatiwala et al., 2006). The shear and bulk viscosity, μ_1 and μ_2, were estimated to be 5×10^6 Pa s, which is in the range of other reported values (Namy et al., 2004).
- *Cell mechanics*: The maximum cellular active stress $p_{\max}$ was prescribed a value of 1.5×10^{-2} dyne/cell, in the range of the experimental data of Shreiber et al. (2003). The parameters θ_1 and θ_2 were estimated to be -0.25 and 0.5, respectively. The average stiffness of a fibroblast is the order of 1 kPa (Nagayama et al., 2004; Schäfer and Radmacher, 2005; Lim et al., 2006), mostly due to the contractile activity and actin filaments (Schäfer and Radmacher, 2005). Based on this data K_{act} was taken as 1 kPa (cell/cm^2)$^{-1}$ and K_{pas} was considered for simplicity to be zero. Finally, it is quite difficult to find quantitative experimental data to fit the parameter λ. Here, λ was given a value of 0.25×10^{-10} cell^{-2}, which leads to a positive value of τ_2, which is a necessary condition for the emergence of pattern.

As for the parameters quantifying the long-range effects, β, h_2, and D_2, two different combinations have been chosen (see Table 1), which, according to the linear stability analysis, give rise to two different types of dispersion relations: a dispersion relation with positive growth rates at arbitrarily large wavenumbers (Fig. 1c) is obtained with the parameter set A, whereas a finite range of unstable modes (Fig. 1b) is found with parameter set B.

Finally, simulations were performed on a 5×5 mm^2 square domain, whose size is of the same order as other simulation works (Manoussaki, 2003).

Table 1 Value of the parameters quantifying long-range effects

		Set A	Set B
β	(cm^2)	0.0	1.0×10^{-3}
h_2	$(cm^4/s(gr/cm^3)^{-1})$	1.0×10^{-8}	1.0×10^{-8}
D_2	(cm^4/s)	0.0	1.0×10^{-8}

6. Numerical results

6.1. Impermeable boundary

Firstly, simulations of the dynamical behaviour of the model have been performed with the parameter set A, which possesses a dispersion relation with an infinite range of unstable modes according to the linear stability analysis. Keeping the size of the domain constant, simulations were implemented with mesh densities ranging from 20×20 to 100×100 quadratic elements and numerous spatially varying random perturbations of the biologically relevant homogeneous steady for the cell density initial conditions.

In all of the cases, a stationary spatial pattern emerged after an initial transitory period. This pattern is irregular, consisting of large convex lacunae of varying size, where the cell density is very low and the volumetric strain is positive, together with a filament-like cellular network, where cells are concentrated and the matrix is under compressive volumetric strain (Fig. 8). The two most distinctive features of the results are: (i) the qualitative form of the pattern does not depend on the initial conditions; (ii) the average diameter of the lacunae, i.e. the wavelength of the pattern is strongly dependent on the mesh since it decreases as the size of the element is refined. Actually, it is possible to verify that the numerically obtained wavelength is always the smallest one that the spatial discretisation is able to reproduce, which we can estimate as approximately 4 times the size of element, for this type of quadratic spatial approximation. Note that these results confirm that, at least with our model, dispersion relations of the type of Fig. 1c yield patterning which degenerates to the mesh-dependent wavelengths, eventually reaching the cellular-level scale on mesh refinement, where continuum models are no longer valid.

The dynamical behaviour of the system is different when the parameter set B is used in the simulations. According to the linear stability analysis, only a finite range of wavenumbers is unstable in this situation and the numerical simulation results no longer depend on the mesh size. In addition, the simulations also illustrate the robustness of the pattern with regard to the different initial conditions, since the qualitative form of the pattern is independent of the initial profile of cell density. Therefore, pattern formation does not result from amplification of the initial conditions, but from self-organising properties of the ECM-cell medium.

Figure 9 shows the spatial distribution of cell density at different points in time. In less than 6 h, the first signs of lacunae formation can be distinctly observed. After 12 h, the lacunae are clearly formed, but their size is still increasing. Within approximately 18 h, the steady state has already emerged and the size and shape of the lacunae and the associated capillary-like cell network do not evolve further. Note the close temporal and spatial similarity between the results of Fig. 9 and *in vitro* experiments of angiogenesis (see Stéphanou et al., 2007 for example).

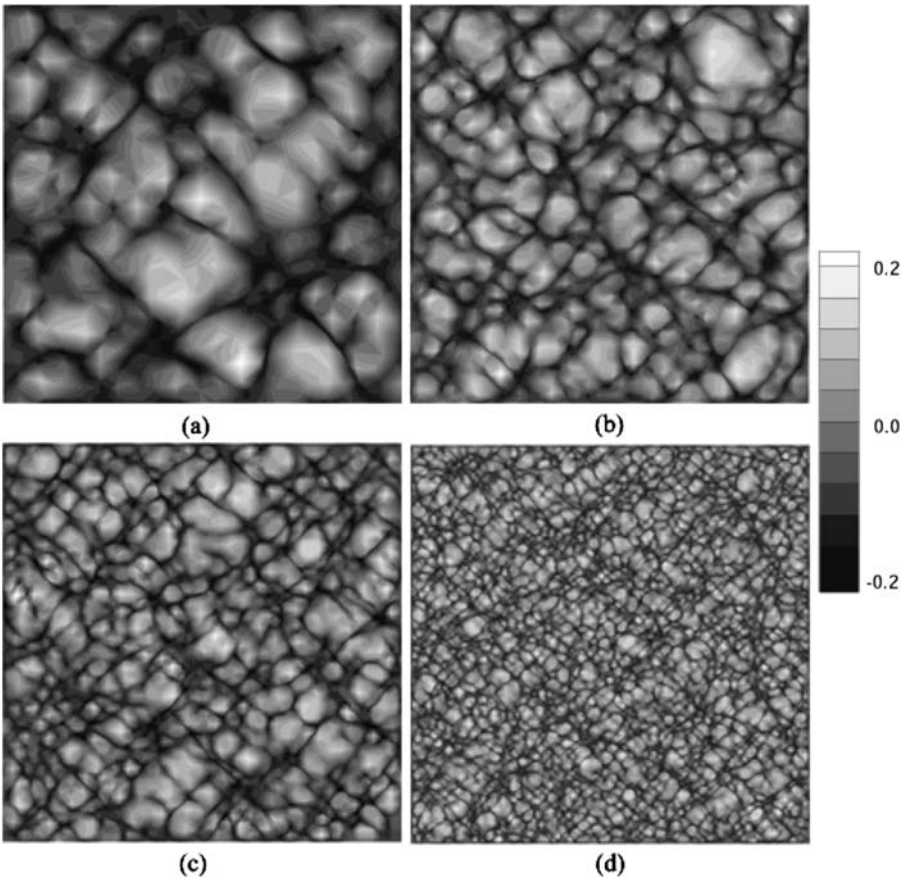

Fig. 8 Steady-state patterns obtained for the volumetric strain θ with the set of parameters A and different mesh sizes. The number of quadratic elements used in each case was: (a) 20×20, (b) 36×36, (c) 50×50, (d) 100×100.

The arrows of Fig. 9 indicate the direction of the displacement of the ECM. As could be expected, lacunae correspond to regions subjected to tensile strains whereas the thin network between lacunae can be identified with areas under compression.

Finally, it is to be noted that the results of this section are not significantly altered when the two different alternatives for the second boundary condition are tested. In other words, if one considers a domain with an impermeable boundary and thus sets that the total flux of cells is zero at the boundary, one can freely choose, at least with our model, between imposing additionally $\nabla n \cdot \boldsymbol{\eta} = 0$ or $\nabla^2 n = 0$ at the boundary to obtain a well-posed problem, since the numerical results do not noticeably depend on this choice.

6.2. Infinite source-like environment

The simulations were repeated with an inhomogeneous Dirichlet boundary condition and the parameter set B (Fig. 10). Remarkably, the results do not change qualitatively through-

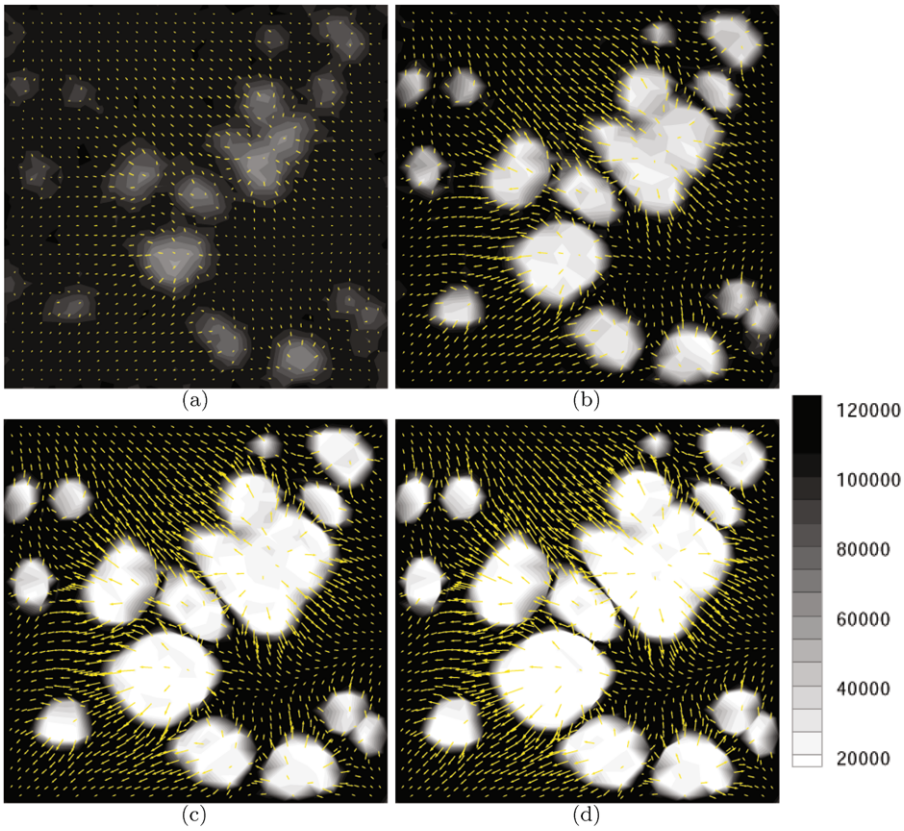

Fig. 9 Evolution of cell density n (cell/cm^2) with the set of parameters B at successive times: (a) 6 h, (b) 12 h, (c) 18 h, and (d) 24 h. The superimposed arrows indicate the direction and amplitude of the local displacement vector **u**, with the arrow length proportional to the vector norm.

out the inner part of the domain, with the shape and size of the lacunae qualitatively similar to those of Fig. 9d. Hence, the Dirichlet boundary condition is responsible solely for an edge effect close to boundary of the domain, where the density of cells is now more uniform, as could be expected. Again, the particular choice for the second boundary condition does not significantly alter the numerical results.

7. Discussion

7.1. The stability analysis

First of all, we note that interpreting condition (31) in terms of the underlying biophysics is far from straightforward, emphasising the need for a modelling approach to understand how cells' mechanical responses impact on biological self-organisation.

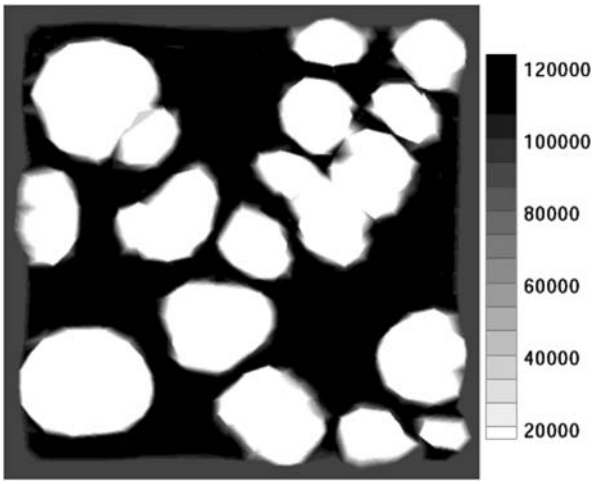

Fig. 10 Cell density n (cell/cm^2) after 24 h obtained with the set of parameters B and an inhomogeneous Dirichlet boundary condition.

It should be mentioned that the linear stability analysis of the general model predicts that spatial disturbances of sufficiently small wavelength are always stable. Thus, typically the model does not degenerate into pattern at the cellular-level scale, where the continuum approach would become invalid. This fine grained degeneration would require the absence of nonlocal cellular forces, or their effective absence in the case where $a_3 \ll 1$, so that a dispersion relation with the form of Fig. 1c emerges. However, we emphasise that the appearance of such a cellular scale pattern must be confirmed by discrete modelling, since it is a scenario outside the range of validity of a continuum model. Nonetheless, our analysis does show when the continuum approximation breaks down, and thus yields necessary conditions for the formation of fine grained patterning.

Analytical conditions for the formation of pattern have been derived. When the nonlocal haptotatic effects or the non-local effects of cell density on the stress $\boldsymbol{\sigma}_{\text{cell}}$ are sufficiently weak, so that $y \stackrel{\text{def}}{=} -3a_1a_3/a_2^2 \ll 1$, we have found that once $\widetilde{h}_1$ is above a critical threshold and $\tau_2 > 0$ pattern appears if cell forces are sufficiently large. Active forces therefore play a critical role in pattern generation. Firstly, consider the saturation and even decrease of cell traction forces at high cell density, quantified by λ and due to contact inhibition plus competition for ECM binding sites (Ferrenq et al., 1997; Namy et al., 2004; Murray, 1989). This must be lower than a threshold value to allow cells to sufficiently deform the matrix and create a non-uniform steady state of the matrix density. Specifically, whenever $\lambda > 1$, and thus $\tau_2 < 0$, no pattern can emerge. Similar results were obtained with other mechanochemical models when the same type of saturation law for cell forces was used (Murray, 1989). Secondly, the magnitude of the active force per cell, quantified by p_0, is also critical; when it is below a certain threshold no pattern can emerge. This is consistent with the mechanism through which pattern is generated, which relies on the deformation of the ECM by the application of cell forces. If cells are not able to initially deform the ECM in a sufficient manner, due to either the low value of the forces they

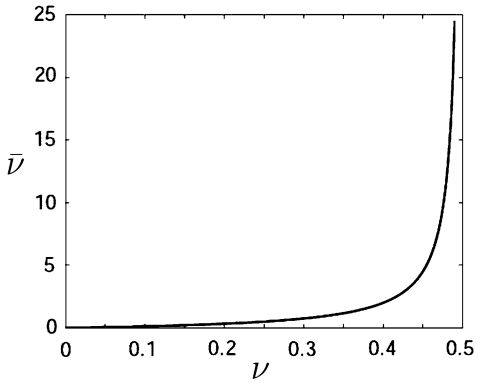

Fig. 11 Dependence of $\bar{\nu}$ upon the Poisson coefficient ν. Observe the asymptotic growth of $\bar{\nu}$ as we approach the incompressible limit, given by $\nu = 0.5$.

are able to exert or the saturation of the active macroscopic cellular stress at high cell densities, patterning cannot proceed.

Another remarkable issue is the equivalent role that local haptotaxis and durotaxis/tensotaxis, quantified respectively by h_1 and M, play in the conditions for biological pattern formation. In all the expressions, h_1 and M appear grouped in the parameter $\widetilde{h}_1 = h_1 + M(1 + \bar{\nu})$, which is designated the *effective haptotaxis coefficient*. Considering (28) and (31) shows that the combined effect of haptotaxis and durotaxis/tensotaxis fosters the growth of pattern, in that once the effective haptotaxis is sufficiently large, further increases always decrease the minimum level of force that cells need to exert to generate pattern. This can be intuitively explained if one considers that the mechanical taxis simply consists of a directed movement of cells according to a gradient of cellular stresses and that such a gradient can instigate or be instigated by a gradient of ECM strains, that in turn, from Eq. (2), are directly related to the ECM density. Hence, it is reasonable that haptotaxis, which depends on gradients of ECM density, has a similar effect on pattern formation as mechanotaxis.

In addition, note that $\widetilde{h}_1$ depends not only on M but on the product $M\bar{\nu}$ as well. Usually soft biological tissues are weakly compressible and have large values of the Poisson coefficient, ν, leading to high values of $\bar{\nu}$ (see Fig. 11). These results stress the role that active mechanosensing can play, not only in the migration of cells, affecting the speed and direction of their movement, but also in cell organisation within soft tissues, where the information gathered by cells by actively probing the mechanical environment can wield a significant influence on their positioning and orientation (Bischofs and Schwarz, 2003; Schwarz and Bischofs, 2005).

Next, it should be noted that because $y \stackrel{\text{def}}{=} -3a_1a_3/a_2^2$ need not tend to zero as the non-local effects tend to zero, the instability region has a singular limit. The parameter space for instability is, in general, very different when small non-local forces are present compared to when no non-local effects are present. Thus, non-local phenomena can have a disproportionate effect on the stability properties of the system. When $a_2 < 0$, this effect is dramatic as the non-local forces prevent arbitrarily large wavenumbers, though it is also present when $a_2 > 0$.

Also, detailed study of special cases shows that the instability conditions can differ significantly from when $a_3 \neq 0 \Leftrightarrow \beta h_2 \neq 0$ (i.e. $y > 0$ and not necessarily small) to when $\beta h_2 = 0$ (i.e. $y = 0$) showing that the interaction of the non-local effects has an substantial influence on system stability. The most relevant of these differences is the upper bound found for p_0 from the instability conditions when $\beta = 0$.

Similar differences are found when considering scenarios with only one long range effect. Remarkably, the cases in which only long range diffusion ($D_2 > 0, h_2 = 0, \beta = 0$) or long range cellular forces ($\beta > 0, D_2 = 0, h_2 = 0$) are active present similar features: either no pattern emerges or, when it does, there is only a finite range of unstable wavenumbers. However, if we try to determine the bifurcation conditions for the situations of only long range haptotaxis ($h_2 > 0, D_2 = 0, \beta = 0$) or the case of no long range effects one can immediately deduce from Eq. (28) that the only possible spatial pattern that can grow has an unbounded interval of unstable modes.

Therefore, assuming the validity of the mechanochemical mechanism on which this model is based, cells need some type of nonlocal behaviour to give rise to spatial biological pattern of finite wavelength and the results indicate that long range diffusion or the application of long range forces by cells are the two mechanisms that by themselves can be responsible for this behaviour. Combinations of two of the three long-range effects contemplated in this work or a potential simultaneous interplay of all three can also drive the emergence of large-scale pattern.

It is to be noted that simpler models than the one proposed in this work can be valid for the study of pattern formation in special cases. For example, it was shown in Murray (2003) that isotropic strain-stimulated cell traction without diffusion is sufficient to form patterns.

Finally, the previous analysis revealed that temporal or spatiotemporal patterns cannot develop in our system, so that the spatial Turing instability the only possible source of symmetry breaking and pattern. In the context of the main application of this modelling framework, i.e. morphogenesis, this is a noteworthy and desirable feature, since such processes rely on the appearance of robust a stationary pattern, which is stable in time.

7.2. The numerical analysis

The first aspect to highlight from the results of the numerical simulations is the consistency found between the linear stability analysis and the finite element simulations. Specifically, self-organisation is either present or absent in the simulations in accordance with the analysis. In addition, when pattern emerges the spatial oscillations are stable in time, as derived analytically. Furthermore, the fact that the qualitative shape of pattern does not depend on the initial conditions indicates that spatial oscillations are not the result of amplification of the initial conditions.

The most remarkable result is obtained when a dispersion relation of the form of Fig. 1c is used in the simulations, since a breakdown of the continuum approximation by fine grain patterning does occur, rather than the sensitivity to initial conditions advocated in other works (Murray, 1989; Manoussaki et al., 1996). So, at least with the proposed model, dispersion relations in which arbitrarily large wavenumbers are unstable always result in spatial pattern with the smallest wavelength that the discretisation is able to reproduce, independently of the initial conditions.

Also, from the results, one can intuitively envisage how instabilities are generated: in regions of the ECM where the concentration of cells is slightly higher than in the surroundings the macroscopic cellular stress $\boldsymbol{\sigma}_{\text{cell}}$ will also be higher, indicating that these cells will pull the neighbouring ECM with a larger traction force. Hence, the ECM will deform with its density increasing in high cellular concentration areas. Due to passive convection, cell concentration will then also increase in such areas, thus initiating an autocatalytic, positive feedback. Only the nonlinear effects of the logistic growth and the saturation of active forces at high cell densities or ECM strain prevent cell density blow-up.

Finally, the numerical results show that changing the zero-flux boundary condition for the cell density to an inhomogeneous Dirichlet boundary condition alters the results close to the boundary, but the qualitative features of the spatial pattern that emerges inside the domain are not significantly altered. Another remarkable issue is the fact that the numerical results are effectively insensitive to the choice of the second boundary condition. This is particularly important if one considers that from a mathematical standpoint this second boundary condition is needed to ensure the well posedness of the problem, but from the point of view of biology, it is difficult to interpret.

7.3. Summary

The objective of this study has been to investigate the self-organisation properties exhibited by the mechanochemical model of Moreo et al. (2008), motivating a detailed linear stability analysis and finite element simulations. The analytical investigations have revealed that the conditions for pattern emergence are singularly dependent on long-range effects. They have also highlighted that haptotaxis and durotaxis/tensotaxis have an equivalent influence on pattern emergence, in turn emphasising the role cell mechanosensing can have in self-organisation. The remarkable pathological dependence on the mesh and the concomitant fine grained patterning for the simulations of systems characterised by dispersion relations with growth rates at infinitely large wavenumbers also reveals an eventual breakdown of the continuum hypothesis.

Acknowledgements

The authors gratefully acknowledge the research support of the Spanish Ministry of Science and Technology through Research Projects DPI2006-14669 and DPI2006-09692 and the FPU graduate research fellowship program. This publication is based on work supported in part by Award No. KUK-C1-013-04, made by King Abdullah University of Science and Technology (KAUST).

Appendix: Non-dimensionalisation

Equations (15)–(16) are obtained from (1), (3), and (2) after appropriate simplifications and non-dimensionalisation. With this aim, we introduce characteristic values for time, T,

space, L, and ECM density, ρ_0, and rescale in the following way:

$$
\begin{aligned}
&x^* = \frac{x}{L}, \qquad t^* = \frac{t}{T}, \qquad n^* = \frac{n}{N}, \qquad \mathbf{u}^* = \frac{\mathbf{u}}{L}, \qquad \rho^* = \frac{\rho}{\rho_0}, \qquad \boldsymbol{\varepsilon}^* = \boldsymbol{\varepsilon},\\
&\theta^* = \theta, \qquad D_1^* = \frac{D_1 T}{L^2}, \qquad D_2^* = \frac{D_2 T}{L^4}, \qquad h_1^* = \frac{h_1 T \rho_0}{L^2}, \qquad h_2^* = \frac{h_2 T \rho_0}{L^4},\\
&M^* = \frac{MET}{N(1+\nu)L^2}, \qquad p_{\text{cell}}^* = \frac{p_{\text{cell}} N(1+\nu)}{E}, \qquad \tau^* = \frac{\tau N(1+\nu)}{E}, \qquad \text{(A.1)}\\
&r_{\max}^* = r_{\max} T, \qquad r^* = rT, \qquad \mu_1^* = \frac{\mu_1(1+\nu)}{ET}, \qquad \mu_2^* = \frac{\mu_2(1+\nu)}{ET},\\
&\lambda^* = \lambda N^2, \qquad \beta^* = \frac{\beta}{L^2}, \qquad K_{\text{act}}^* = \frac{K_{\text{act}} N(1+\nu)}{E}, \qquad K_{\text{pas}}^* = \frac{K_{\text{pas}} N(1+\nu)}{E}.
\end{aligned}
$$

References

Alastrué, V., Rodríguez, J.F., Calvo, B., Doblaré, M., 2007. Structural damage models for fibrous biological soft tissues. Int. J. Solids Struct. 44, 5894–5911.

Barocas, V.H., Moon, A.G., Tranquillo, R.T., 1995. The fibroblast-populated collagen microshpere assay of cell traction force—Part 2: Measurement of the cell traction parameter. J. Biomech. Eng. 117, 161–170.

Barrett, J.W., Blowey, J.F., Garcke, H., 1999. Finite element approximation of the Cahn–Hilliard equation with degenerate mobility. SIAM J. Numer. Anal. 37, 286–318.

Bischofs, I.B., Schwarz, U.S., 2003. Cell organization in soft media due to active mechanosensing. Proc. Natl. Acad. Sci. U.S.A. 100, 9274–9279.

Collen, A., Koolwijk, P., Kroon, M., van Hinsbergh, V.W.M., 1998. Influence of fibrin structure on the formation and maintenance of capillary-like tubules by human microvascular endothelial cells. Angiogenesis 2, 153–165.

Conway, E.M., Collen, D., Carmeliet, P., 2001. Molecular mechanisms of blood vessel growth. Cardiovasc. Res. 49, 507–521.

Cross, M.C., Hohenberg, P.C., 1993. Pattern formation outside of equilibrium. Rev. Mod. Phys. 65, 851–1112.

Cruywagen, G.C., Maini, P.K., Murray, J.D., 1997. Biological pattern formation on two-dimensional spatial domains: a nonlinear bifurcation analysis. SIAM J. Appl. Math. 57, 1485–1509.

Cullinane, D.M., Salisbury, K.T., Alkhiary, Y., Eisenberg, S., Gerstenfeld, L., Einhorn, T.A., 2003. Effects of the local mechanical environment on vertebrate tissue differentiation during repair: does repair recapitulate development? J. Exp. Biol. 206, 2459–2471.

Dassault Systèmes Simulia Corp., 2006. Abaqus user's Manual, v. 6.6. Providence, RI, USA.

Davidson, D., 1983a. The mechanism of feather pattern development in the chick. I. The time of determination of feather position. J. Embryol. Exp. Morph. 74, 245–259.

Davidson, D., 1983b. The mechanism of feather pattern development in the chick. II. Control of the sequence of pattern formation. J. Embryol. Exp. Morph. 74, 261–273.

Dickinson, R.B., Tranquillo, R.T., 1993. A stochastic model for adhesion-mediated cell random motility and haptotaxis. J. Math. Biol. 31, 563–600.

Discher, D.E., Janmey, P., Wang, Y., 2005. Tissue cells feel and respond to the stiffness of their substrate. Science 310, 1139–1143.

Doblaré, M., García-Aznar, J.M., 2005. On the numerical modelling of growth, differentiation and damage in structural living tissues. Arch. Comput. Methods Eng. 11, 1–45.

Engler, A., Bacakova, L., Newman, C., Hategan, A., Griffin, M., Discher, D., 2004. Substrate compliance versus ligand density in cell on gel responses. Biophys. J. 86, 617–628.

Feng, X., Prohl, A., 2003. Analysis of a fully-discrete finite element method for the phase field model and approximation of its sharp interface limits. SIAM J. Numer. Anal. 73, 541–567.

Ferrenq, I., Tranqui, L., Vailhe, B., Gumery, P.Y., Tracqui, P., 1997. Modelling biological gel contraction by cells: mechanocellular formulation and cell traction force quantification. Acta. Biotheor. 45, 267–293.

Field, R.J., Burger, M., 1985. Oscillations and Traveling Waves in Chemical Systems. Wiley, New York.

FitzHugh, R., 1961. Impulses and physiological states in theoretical models of nerve membrane. Biophys. J. 1, 445–466.

Flesselles, J.M., Simon, A.J., Libchaber, A., 1991. Dynamics of one-dimensional interfaces: an experimentalists' overview. Adv. Phys. 40, 1–51.

Garikipati, K., Arruda, E.M., Grosh, K., Narayanan, H., Calve, S., 2004. A continuum treatment of growth in biological tissue: the coupling of mass transport and mechanics. J. Mech. Phys. Solids 52, 1595–1625.

Ghosh, K., Pan, Z., Guan, E., Ge, S., Liu, Y., Nakamura, T., Ren, X., Rafailovich, M., Clark, R.A.F., 2007. Cell adaptation to a physiologically relevant ecm mimic with different viscoelastic properties. Biomaterials 28, 671–679.

Gierer, A., Meinhardt, H., 1972. A theory of biological pattern formation. Kybernetik 12, 30–39.

Glass, L., Hunter, P., 1990. There is a theory of heart. Physica D 43, 1–16.

Hodgkin, A.L., Huxley, A.F., 1952. A quantitative description of membrane current and its application to conduction and excitation in nerve. J. Physiol. (London) 117, 500–544.

Holmes, M.J., Sleeman, B.D., 2000. A mathematical model of tumour angiogenesis incorporating cellular traction and viscoelastic effects. J. Theor. Biol. 202, 95–112.

Hughes, T.J.R., 2000. The Finite Element Method, 1st edn. Dover, New York.

Hunter, P., Pullan, A., Smaill, B., 2003. Modeling total heart function. Annu. Rev. Biomed. Eng. 5, 147–177.

Khatiwala, C.B., Peyton, S.R., Putnam, A.J., 2006. Intrinsic mechanical properties of the extracellular matrix affect the behavior of pre-osteoblastic MC3T3-E1 cells. Am. J. Physiol. Cell Physiol. 290, 1640–1650.

Lim, C.T., Zhou, E.H., Quek, S.T., 2006. Mechanical models for living cells—a review. J. Biomech. 39, 195–216.

Lo, C., Wang, H., Dembo, M., Wang, Y., 2000. Cell movement is guided by the rigidity of the substrate. Biophys. J. 79, 144–152.

Maini, P.K., Myerscough, M.R., Winters, K.H., Murray, J.D., 1991. Bifurcating spatially heterogeneous solutions in chemotaxis model for biological pattern generation. Bull. Math. Biol. 53, 701–719.

Manoussaki, D., 2003. A mechanochemical model of angiogenesis and vasculogenesis. ESAIM: Math. Model. Numer. Anal. 37, 581–599.

Manoussaki, D., Lubkin, S.R., Vernon, R.B., Murray, J.D., 1996. A mechanical model for the formation of vascular networks in vitro. Acta Biotheor. 44, 271–282.

Meinhardt, H., Prusinkiewicz, P., Fowler, D.R., 2003. The Algorithmic Beauty of Sea Shells, 3rd edn. Springer, Berlin.

Mittenthal, J.E., Mazo, R.M., 1983. A model for shape generation by strain and cell-cell adhesion in the epithelium of an arthropod leg segment. J. Theor. Biol. 100, 443–483.

Miura, T., Shiota, K., Morriss-Kay, G., Maini, P.K., 2006. Mixed-mode pattern in doublefoot mutant mouse limb—Turing reaction–diffusion model on a growing domain during limb development. J. Theor. Biol. 240, 562–573.

Moloney, J.V., Newell, A.C., 1990. Nonlinear optics. Physica D 44, 1–37.

Moreo, P., García-Aznar, J.M., Doblaré, M., 2008. Modeling mechanosensing and its effect on the migration and proliferation of adherent cells. Acta Biomater. 4, 613–621.

Murray, J.D., 1981a. On pattern formation mechanisms for lepidopteran wing patterns and mammalian coat markings. Philos. Trans. R. Soc. Lond. B 295, 473–496.

Murray, J.D., 1981b. A pre-pattern formation mechanism for animal coat markings. J. Theor. Biol. 88, 143–163.

Murray, J.D., 1989. Mathematical Biology, 1st edn. Springer, Berlin.

Murray, J.D., 2003. On the mechanochemical theory of biological pattern formation with application to vasculogenesis. C. R. Biol. 326, 239–252.

Murray, J.D., Oster, G.F., 1984. Generation of biological pattern and form. IMA J. Math. Appl. Med. Biol. 1, 51–75.

Murray, J.D., Maini, P.K., Tranquillo, R.T., 1988. Mechanochemical models for generating biological pattern and form in development. Phys. Rep. 171, 59–84.

Nagayama, M., Haga, H., Takahashi, M., Saitoh, T., Kawabata, K., 2004. Contribution of cellular contractility to spatial and temporal variations in cellular stiffness. Exp. Cell Res. 300, 396–405.

Nagumo, J.S., Arimoto, S., Yoshizawa, S., 1962. An active pulse transmission line simulating nerve axon. Proc. IRE 50, 2061–2071.
Namy, P., Ohayon, J., Tracqui, P., 2004. Critical conditions for pattern formation and in vitro tubulogenesis driven by cellular traction fields. J. Theor. Biol. 202, 103–120.
Oster, G.F., Murray, J.D., Harris, A.K., 1983. Mechanical aspects of mesenchymal morphogenesis. J. Embryol. Exp. Morph. 78, 83–125.
Park, J.Y., Gemmell, C.H., Davies, J.E., 2001. Platelet interactions with titanium: modulation of platelet activity by surface topography. Biomaterials 22, 2671–2682.
Pavlin, D., Dove, S.B., Zadro, R., Gluhak-Heinrich, J., 2000. Mechanical loading stimulates differentiation of periodontal osteoblasts in a mouse osteoinduction model: effect on type I collagen and alkaline phosphatase genes. Calcif. Tissue Int. 67, 163–172.
Pelham, R.J., Wang, Y., 1997. Cell locomotion and focal adhesions are regulated by substrate flexibility. Proc. Natl. Acad. Sci. U.S.A. 94, 13,661–13,665.
Peña, E., Calvo, B., Martínez, M.A., Doblaré, M., 2007. An anisotropic visco-hyperelastic model for ligaments at finite strains formulation and computational aspects. Int. J. Solids Struct. 44, 760–778.
Perumpanani, A.J., Byrne, H.M., 1999. Extracellular matrix concentration exerts selection pressure on invasive cells. Eur. J. Cancer 35, 1274–1280.
Peyton, S.R., Putnam, A.J., 2005. Extracellular matrix rigidity governs smooth muscle cell motility in a biphasic fashion. J. Cell Physiol. 204, 198–209.
Ramtani, S., 2004. Mechanical modelling of cell/ECM and cell/cell interactions during the contraction of a fibroblast-populated collagen microsphere: theory and model simulation. J. Biomech. 37, 1709–1718.
Schäfer, A., Radmacher, M., 2005. Influence of myosin II activity on stiffness of fibroblast cells. Acta Biomater. 1, 273–280.
Schwarz, U.S., Bischofs, I.B., 2005. Physical determinants of cell organization in soft media. Med. Eng. Phys. 27, 763–772.
Shreiber, D.I., Barocas, V.H., Tranquillo, R.T., 2003. Temporal variations in cell migration and traction during fibroblast-mediated gel compaction. Biophys. J. 84, 4102–4114.
Stéphanou, A., Meskaoui, G., Vailhé, B., Tracqui, P., 2007. The rigidity of fibrin gels as a contributing factor to the dynamics of *in vitro* vascular cord formation. Microvas. Res. 73, 182–190.
Turing, A.M., 1952. The chemical basis of morphogenesis. Philos. Trans. R. Soc. Lond. B 237, 37–72.
Vailhé, B., Vittet, D., Feige, J.J., 2001. In vitro models of vasculogenesis and angiogenesis. Lab. Invest. 81, 439–452.
Wells, G.N., Kuhl, E., Garikipati, K., 2006. A discontinuous Galerkin method for the Cahn–Hilliard equation. J. Comput. Phys. 218, 860–877.
Wolpert, L., 1969. Positional information and the spatial pattern of cellular differentiation. J. Theor. Biol. 25, 1–47.
Yang, L., Dolnik, M., Zhabotinsky, A.M., Epstein, I.R., 2002. Pattern formation arising from interactions between Turing and wave instabilities. J. Chem. Phys. 117, 7259–7265.